Technical note: Dispersion of cooking-generated aerosols from an urban street canyon

Shang Gao[1], Mona Kurppa[2], Chak K. Chan[1], and Keith Ngan[1]

[1]School of Energy and Environment, City University of Hong Kong, Kowloon, Tat Chee Avenue, Hong Kong
[2]Atmospheric Composition Research, Finnish Meteorological Institute, Helsinki, Finland

Correspondence: Chak K. Chan (chak.k.chan@cityu.edu.hk); Keith Ngan (keith.ngan@cityu.edu.hk)

Abstract. The dispersion of cooking-generated aerosols from an urban street canyon is examined with building-resolving computational fluid dynamics (CFD). Using a comprehensive urban CFD model (PALM) with a sectional aerosol module (SALSA), emissions from deep frying and boiling are considered for near-ground and elevated sources. With representative choices of the source flux, the inclusion of aerosol dynamic processes decreases the mean canyon-averaged number concentration by $15-40\%$ for cooking emissions, whereas the effect is significantly weaker for traffic-generated aerosols. The effects of deposition and coagulation are comparable for boiling, but coagulation dominates for deep frying. Deposition is maximised inside the leeward corner vortices, while coagulation increases away from the source. The characteristic timescales are invoked to explain the spatial structure of deposition and coagulation. In particular, the relative difference between number concentrations for simulations with and without coagulation are strongly correlated with the ageing of particles along fluid trajectories or the mean tracer age. It is argued that, for a specific emission spectrum, the qualitative nature of the aerosol dynamics within urban canopies is determined by the ratio of the aerosol timescales to the relevant dynamical timescale (e.g. the mean age of air).

1 Introduction

Computational fluid dynamics (CFD) is a well-established tool for studying urban pollutant dispersion (e.g. Rivas et al., 2019). By including an explicit representation of buildings, urban flows can be simulated more accurately than is possible with coarse-resolution mesoscale atmospheric models (Park et al., 2015) or semi-analytical solutions like the classical Gaussian plume model (Melli and Runca, 1979). Most urban CFD studies assume neutral (uniform density) flow and passive scalar dynamics. In recent years, however, the accuracy of urban CFD models has been increased through the inclusion of additional physical processes such as solar heating (Nazarian and Kleissl, 2016) and gas-phase chemistry (Zhong et al., 2015).

One extension that has received relatively little attention is the inclusion of aerosol dynamic processes. The dynamics of urban aerosols differs from that of completely passive, neutrally buoyant particles because their evolution is affected by processes such as condensation, coagulation, deposition and nucleation (Seinfeld and Pandis, 2016); the importance of coagulation and deposition for urban nanoparticles has been noted by Karl et al. (2016). Since particulate matter poses potentially severe risks to human health (Greene and Morris, 2006), improved modelling of urban aerosols is desirable. Urban CFD studies of

aerosols have examined ultra-fine particles (Nikolova et al., 2011; Scungio et al., 2013), PM2.5 evolution (Zhang et al., 2011) and aerosol-chemistry coupling (Kim et al., 2012, 2019) arising from vehicular particle sources. Deposition is usually the only aerosol process included in urban CFD models as it is often taken to be the most important loss process of ultrafine particles emitted by traffic (Kumar et al., 2011; Kim et al., 2019). Nevertheless, additional aerosol processes have been incorporated into global and regional atmospheric models using sectional aerosol modules in which the distribution of particles is repre-

30 sented with a set of discrete size bins (e.g. Gong et al., 2002). The sectional aerosol module SALSA (Kokkola et al., 2008) was coupled to the PALM urban CFD model by Kurppa et al. (2019) (hereafter K19), yielding good agreement with in situ measurements of the aerosol size spectrum.

Although numerical modelling of urban aerosols has focused on emissions from motor vehicles, other sources, such as ships (Ackerman et al., 1995) and factories (Purba and Tekasakul, 2012) also exist. Cooking-generated aerosols from restaurants can have a surprisingly large effect: in situ measurements conducted in a densely urbanised neighbourhood of Hong Kong

35 show that the contribution of cooking emissions to organic aerosols may exceed that of motor vehicles (Lee et al., 2015; Liu et al., 2018). Despite their importance, little is known about the dynamics of cooking-generated aerosols in the outdoor environment; current understanding relies on in situ measurements and idealised laboratory experiments (Gao et al., 2015). The dispersion of cooking- and traffic-generated aerosols differ in two key respects. First, the size distribution of cooking emissions

40 is shifted towards smaller particles as the proportion of particles with a diameter of O(10 nm) or less is much larger (See and Balasubramanian, 2006; Yeung and To, 2008). Hence the relative importance of the aerosol processes may change. Second, the particles are emitted from kitchen exhaust ducts, which may be located near the ground or far above it. Given that the dispersion of passive scalars is sensitive to the emission location (Huang et al., 2015; Duan et al., 2019), the aerosol dynamics and concentrations may be strongly affected.

45 In this paper, the dispersion of cooking-generated aerosols from a street canyon is analysed with large-eddy simulation (LES) and a sectional aerosol module. After reviewing the methodology (Sect. 2), results are presented for several idealised but generic emission scenarios, e.g. traffic, deep frying and cooking emissions (Sect. 3). The aerosol dynamic processes are analysed in terms of the underlying aerosol timescales in Sect. 4 so as to highlight the key mechanisms. The sensitivity to factors such as the source strength and background aerosol concentrations is considered in Sect. 5. The robustness of the key

50 findings, and the representativeness of the emission scenarios, is discussed in Sect. 6. Conclusions are given in Sect. 7.

2 Methodology

For simplicity, the dynamical core of the CFD model and the aerosol module are described separately.

2.1 Numerical formulation

2.1.1 PALM

The parallelized large-eddy simulation model (PALM) (Maronga et al., 2015) is an LES model based on the non-hydrostatic, filtered, incompressible Navier-Stokes equations. The 1.5-order Deardorff subgrid-scale (SGS) scheme (Deardorff, 1980) is used to parameterize SGS turbulent fluxes. Fifth-order differencing (Wicker and Skamarock, 2002) is combined with third-order Runge-Kutta time-stepping (Williamson, 1980). While LES is more computationally expensive than the Reynolds-averaged Navier–Stokes (RANS) equations, the inclusion of transient dynamics allows for nonlinear aerosol processes (cf. Sec. 5.2) to be represented more accurately. With a steady model like RANS, temporal fluctuations are neglected, thereby necessitating a turbulence parameterisation for the aerosol dynamics.

2.1.2 SALSA

SALSA includes representations of condensation, coagulation, nucleation and dry deposition (Kokkola et al., 2008). Following K19, only dry deposition, coagulation and condensation are retained. Nucleation, which is most relevant in the immediate vicinity of the source (Rönkkö et al., 2007), can be treated by modifying the emissions (Ketzel and Berkowicz, 2004) and is not considered in this work. Details on the implementation are given in Appendix A. Briefly, deposition removes particles near surfaces: the deposition velocity is non-zero within the first grid box at a surface, e.g. from $z = 0$ to $z = \Delta z$ (cf. Fig. 13a); away from the surface, only gravitational settling occurs. Coagulation coalesces smaller particles into larger ones, decreasing the number concentration but shifting the size distribution; condensation of gases onto particles gases changes the aerosol concentration. As with other sectional models, the parameterisations depend on the particle size. SALSA divides the size distribution into several subranges, each of which is discretised into a specified number of size bins based on the particle diameter, D_p. We adopt the same partitioning as K19: in subrange 1, $D_p \in [3 \text{ nm}, 50 \text{ nm}]$; in subrage 2, $D_p >50$ nm. The particle number in each size bin, n_i, is a prognostic variable. The total particle number $N = \sum_i n_i$.

Particles are introduced via injection of a specific component or through condensation of gaseous components. The chemical components include organic carbon (OC), black carbon (BC), sulfuric acid (H_2SO_4), nitric acid (HNO_3), ammonium (NH_3), sea salt, dust and water (H_2O). Subrange 1 includes OC, H_2SO_4, HNO_3 and NH_3 only, which are assumed to be internally mixed; subrange 2 includes all the chemical components. Gaseous components, namely H_2SO_4, HNO_3, NH_3, semi-volatile (SVOCs) and non-volatile organics (NVOCs), may condense onto particles; however, gas phase chemical reactions are excluded.

2.2 Configuration

2.2.1 PALM

An idealised single street canyon of unit aspect ratio, i.e. with dimensional building height $H = 20$ m and width $W = 20$ m, is located at the centre of the computational domain (Fig. 1a). The domain has dimensions $5H$, $2H$ and $5H$ in the streamwise

(x), spanwise (y) and vertical (z) directions, respectively; the spanwise extent is somewhat limited but comparable to that

85   of previous studies (e.g. Baik et al., 2007; Duan et al., 2019). The uniform, isotropic grid spacing $\Delta = 1$ m. The timestep, $\Delta t_{\text{PALM}} \sim 0.1$ s.
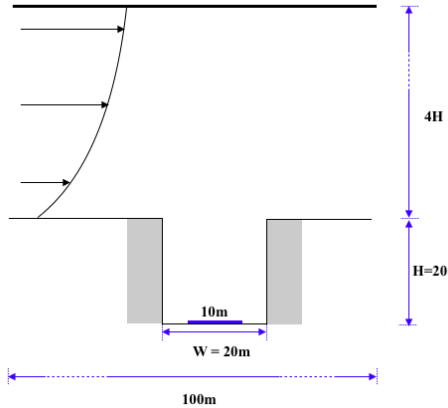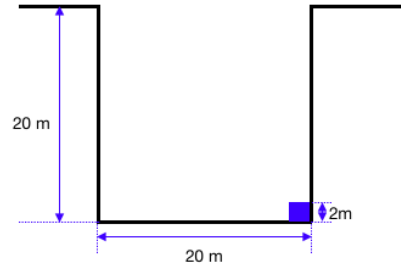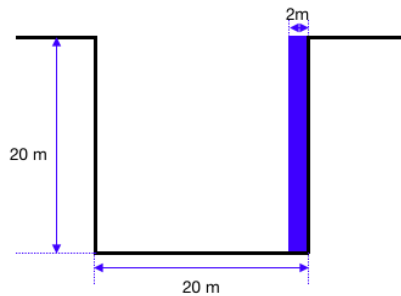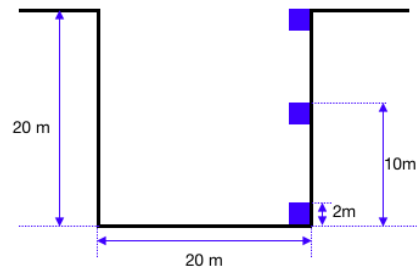
Figure 1. Schematic representations in the $x - z$ plane (at the midplane $y/W = 1$) of the computational domain and pollutant sources: **(a)** ground-level traffic emissions; **(b)** near-ground cooking emissions; **(c)** column cooking emissions; **(d)** isolated cooking emissions. The emission scenarios are defined in Table 1. For clarity, the streamwise position of the cooking sources has beeen shifted.

The boundary conditions follow previous studies. For the velocity, cyclic boundary conditions are applied in the streamwise and spanwise directions, free slip at the top, and no slip at all solid surfaces. For scalar quantities (including the particle number in each size bin), there are cyclic boundary conditions in the spanwise direction and Dirichlet (e.g. $n_i = 0$) in the streamwise

90   direction. The flow is driven by an external pressure gradient, dp/dx = -0.0006 $\text{Pa}\,\text{m}^{-1}$. This value has been widely used in
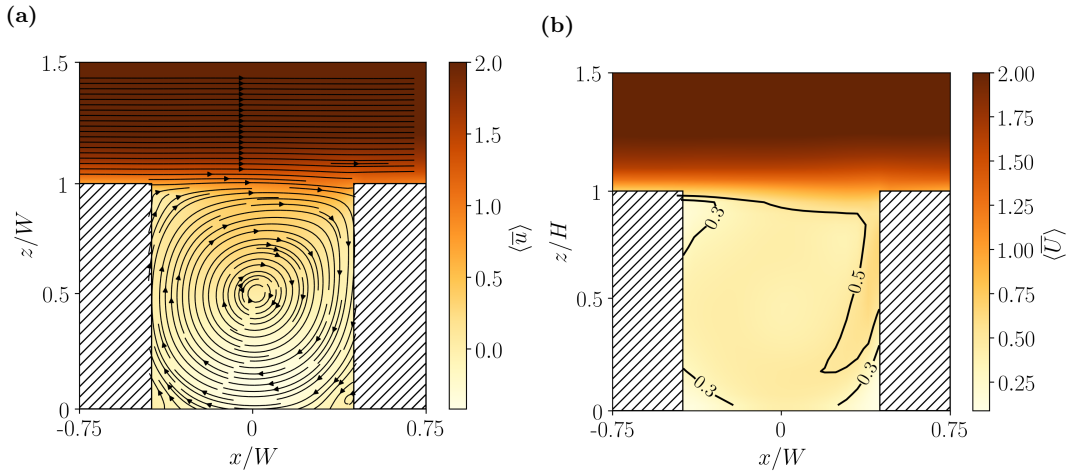
Figure 2. Spatial structure of the mean flow in the $x-z$ plane: **(a)** streamwise velocity component, u $(\mathrm{m\,s^{-1}})$; **(b)** wind speed, U $(\mathrm{m\,s^{-1}})$.

previous CFD studies (e.g. Duan et al., 2019); it yields a streamwise velocity $U \sim 3\mathrm{ms^{-1}}$ at $z/H = 2.5$. The simulations are conducted under neutral conditions with the temperature fixed at 300 K.

The configuration described above differs in several respects from K19. First, an idealised street canyon is used in place of realistic topography within a neighbourhood-scale domain. Second, there is uniform grid spacing rather than a stretched grid. Third, the computational lid height of $5H$ is decreased from $13H_{\mathrm{avg}}$, where H_{avg} is the mean building height.

The model was spun-up for 1000 s in order to attain a statistically steady flow (as determined from the mean streamwise velocity within the canyon). Subsequently particle emission commenced and the model was run for another 5000 s. Data collected during the last 3000 s (with an output interval of 10 s) are analyzed in this study. During the 3000 s sampling period, the number concentration also reaches statistical distribution: the ratio of the standard deviation to the mean is around 6% The time average is denoted by the overbar. The spanwise average is denoted by $\langle \cdot \rangle$ and the canyon average by $\langle \rangle_C$.

Figure 2 shows mean streamlines and wind speed in the $x-z$ plane. The picture is consistent with the many numerical studies of unit-aspect-ratio street-canyon flow. In particular, there is a large central vortex and smaller canyon vortices. Although the corner vortices are not defined as clearly as in higher resolution simulations (e.g. Duan et al., 2019), recirculations clearly exist within the bottom corners. Ramifications of the streamline topology are considered in Sect. 3.

2.2.2 SALSA

Version 4481 of SALSA is used. Following K19, there are five size bins for each of the two subranges. As the current study is concerned with idealised emission scenarios, the background number concentration for the ith size bin, $n_{b,i} = 0$; the sensitivity to $n_{b,i}$ is examined in Sect. 5.1. As in K19, the SALSA timestep $\Delta t_{\mathrm{SALSA}} = 1$ s in all cases. The three aerosol processes in SALSA (coagulation, condensation and deposition) may be activated or deactivated independently of each other.

Pollutants are emitted from uniform area sources. Since aerosol emissions are handled by SALSA rather than PALM, pollutants are subjected to aerosol dynamic processes before being transported and advected by PALM. Two basic source types are considered: (i) ground-level traffic; and (ii) cooking emissions from one side of a street canyon. In the former case, a uniform area source is located at the bottom of the canyon. In the latter case, the sources, which cover a portion of the walls facing the street, are located at the roadside (Fig. 1b); between the ground and the roof level (Fig. 1c); and at the bottom, middle or top floors (Fig. 1d). No attempt is made to represent exhaust ducts. These sources represent roadside and elevated (aligned in a column or else isolated) kitchens. In addition, there are two possible cooking modes, namely deep frying and boiling: both are considered as their emission spectra are rather different (Fig. 3).

2.2.3 Emission scenarios

For each source type, the emission spectra and source flux $(\mathrm{m}^{-2}\,\mathrm{s}^{-1})$ must be specified. Values that are broadly representative of large cities are chosen for the latter. The sensitivity to the net source flux is quantified in Sect. 5.2.

1. *Ground-level traffic (Case TR).* The emission factor for the number of particles emitted by a vehicle per unit distance travelled was estimated to be $3.0 \times 10^{14}\,\mathrm{km}^{-1}\,\mathrm{veh}^{-1}$ (Fujitani et al., 2020). A traffic volume of 1000 vehicles per hour, which corresponds to moderately heavy traffic within a city centre is assumed. The total particle flux (s^{-1}), T_p, is obtained from the emission factor and the length of the street, i.e. $T_p = \epsilon L$, whence the source flux $Q = T_p/A$, where A is the area covered by the traffic.

2. *Cooking emissions.* The emission factors for the number of particles emitted per unit time by a kitchen of unit volume were estimated to be $3.75 \times 10^{10}\,\mathrm{m}^{-3}\,\mathrm{s}^{-1}$ and $4.31 \times 10^{9}\,\mathrm{m}^{-3}\,\mathrm{s}^{-1}$, for deep frying and boiling, respectively. These values are derived from data for reference kitchens with a volume of $\sim 20\,\mathrm{m}^3$; it is assumed that no particles are trapped indoors. The total particle flux (s^{-1}) is obtained from the emission factor and the volume of the kitchens, i.e. $T_p = n\epsilon V$, where V is the volume and n is the number of kitchens. It is assumed for simplicity that particles are emitted uniformly over the external face of the restaurant. The source flux follows from normalisation by A, the area of the kitchen face parallel to the canyon axis. The indoor-outdoor exchange is entirely one-way: particles escape from the kitchens to the outdoor environment but no particles travel in the opposite direction.

The source specification depends on the emission scenario (Table 1):

 – *Near-ground emissions (Case NG).* It is assumed that each roadside kitchen has dimensions $4\,\mathrm{m} \times 2\,\mathrm{m} \times 2\,\mathrm{m}$, with the longest side being parallel to the street. Hence the total particle flux equals the combined emissions from 10 restaurants.

 – *Column emissions (Case CO).* There are a total of five elevated kitchens between the bottom and top floors. The kitchens may be taken to be domestic rather than commercial and of smaller dimensions, namely $2\,\mathrm{m} \times 2\,\mathrm{m} \times 4\,\mathrm{m}$. For simplicity, the combined emissions from the separate kitchens are represented by a continuous column source.

 – *Isolated emissions (Case I).* Only a single elevated kitchen is considered. It has dimensions $2\,\mathrm{m} \times 2\,\mathrm{m} \times 4\,\mathrm{m}$.
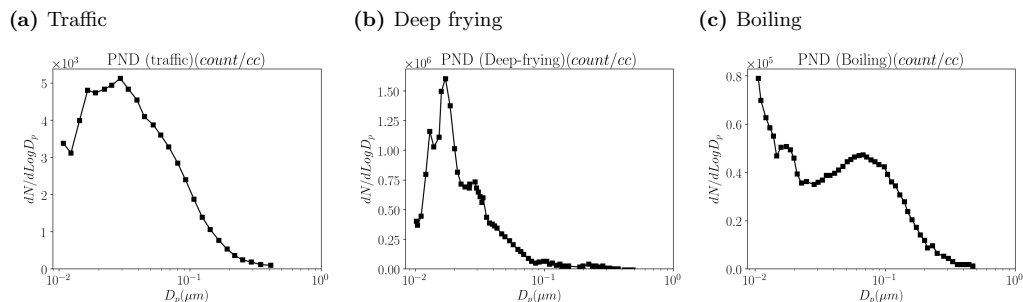
Figure 3. Reference emission spectra: **(a)** traffic (Janhäll et al., 2004); **(b)** deep frying (See and Balasubramanian, 2006); **(c)** boiling (See and Balasubramanian, 2006). The reference spectra are scaled in order to obtain emission spectra for the scenarios of Table 1.

Emission spectra are obtained by scaling the reference spectra (Fig. 3); the contribution of a specific size bin is determined by T_p and the emission spectrum. No attempt is made to represent the kitchen ventilation system; hence all indoor aerosol processes are excluded. The scaling factor for a size bin is given by the ratio of the integral of the emission spectrum over the size bin to the integral over the entire spectrum. Note that, for a kitchen of identical size, deep frying generates nearly 10 times as many particles as does boiling. In addition, more small particles are generated for deep frying: the proportion of nanoparticles in the 1 nm to 100 nm range increases from 65% to 90% and the mean diameter decreases from 57.4 nm to 26.5 nm (See and Balasubramanian, 2006; Yeung and To, 2008). However, the boiling spectrum peaks at a smaller diameter.

The emission scenarios described above are summarised in Table 1.

Several assumptions are required to specify the particle emissions from cooking; their validity is discussed in Sec. 6. The gaseous emissions are specified in Appendix B: in particular, the chemical compositions (Table B-1) and emission factors (Table B-2) are listed.

Table 1. Emission scenarios for the area sources illustrated in Fig. 1. The dimensions of the area sources are expressed in terms of the canyon dimensions (W, L, H) when the source extends along the full extent of the canyon in a given direction, and (w, l, h) otherwise. For the isolated cooking emissions, $z_0/H \in \{0.05, 0.50, 0.95\}$.

Case	Type	Location	Source dimensions
TR	Traffic	Ground level (centred at $x/W = 0$)	$w = 10$ m, L
NG-D	Deep frying	Near-ground	L, $h = 2$ m
NG-B	Boiling	Near-ground	L, $h = 2$ m
CO-D	Deep frying	Column (centred at $y/W = 1$)	$l = 2$ m, H
CO-B	Boiling	Column (centred at $y/W = 1$)	$l = 2$ m, H
I-D-z_0	Deep frying	Isolated (centred at $y/W = 1, z/H = z_0$)	$l = 2$ m, $h = 2$ m
I-B-z_0	Boiling	Isolated (centred at $y/W = 1, z/H = z_0$)	$l = 2$ m, $h = 2$ m

2.3 Validation

Several validation tests have been performed. First, the mean velocity statistics are validated against measurements of flow over parallel unit-aspect-ratio streets canyons (Brown et al., 2001). Second, passive scalar statistics are also validated (Pavageau and Schatzmann, 1999). Finally, the performance of the coupled PALM-SALSA model is compared to previous studies (Kumar et al., 2008; Kurppa et al., 2019).

With respect to the uncoupled CFD model, vertical profiles of the mean streamwise velocity u show good agreement with the measurements at different streamwise locations and $z/H \leq 1.5$ when the PALM configuration of Sec. 2.2.1 is used. Standard validation metrics (Appendix C) confirm that the validation is successful: the normalised mean square error $NMSE \sim 0.01 - 0.04$, fractional bias $FB \sim 0.02$ and correlation coefficient $R \sim 0.99$. For a perfect validation, $NMSE = FB = 0$ and $R = 1$. The agreement is comparable to previous numerical studies (Cui et al., 2004; Duan et al., 2019). Passive scalar statistics for a ground-level line source (see Sec. 2.3 for configuration details) also show good agreement. For example, $NMSE = 0.07$ and $FB = 0.02$ (cf. Fig. C-1). We conclude that PALM is capable of simulating the mean flow and an accompanying passive scalar.

With respect to the coupled PALM-SALSA model, vertical profiles of aerosol number concentration are validated against evening measurements made within a real street canyon in Cambridge, UK (Kumar et al., 2008). For simplicity, the computational domain is focused on this street canyon: no other buildings are included. In particular, a single street canyon of $167 \text{ m} \times 12 \text{ m} \times 12 \text{ m}$ is centred inside a domain of $167 \text{ m} \times 60 \text{ m} \times 60 \text{ m}$. For consistency with the evening measurements, the temperature is fixed at 274 K. Using the background concentrations and traffic counts of Kumar et al. (2008), emissions from the street canyon only are considered. Aside from the computational domain and source specification, the distribution of size bins is adjusted to match PALM and SALSA configurations follow Sec. 2.2. Vertical profiles of the aerosol number concentration are compared in Fig. 5. Compared to K19, the current LES shows improved agreement with in situ measurements for $z/H \lesssim 0.6$, though there are fairly large errors in both cases. The improved agreement may be fortuitous inasmuch as the present validation neglects emissions from outside the street canyon; nevertheless, the present configuration simulates the aerosol distribution in the real urban environment at least as well.

3 Results

3.1 Traffic and near-ground cooking emissions

To highlight the influence of the emission spectrum, we begin by comparing the aerosol number concentration fields generated by traffic and roadside restaurants, i.e. emission scenarios TR, NG-D and NG-B (Table 1). Fig. 6 plots spanwise averages of the dimensionless mean concentrations,

$$\overline{N_*} = \frac{\overline{N} U_{\text{ref}} H L}{T_p}, \tag{1}$$
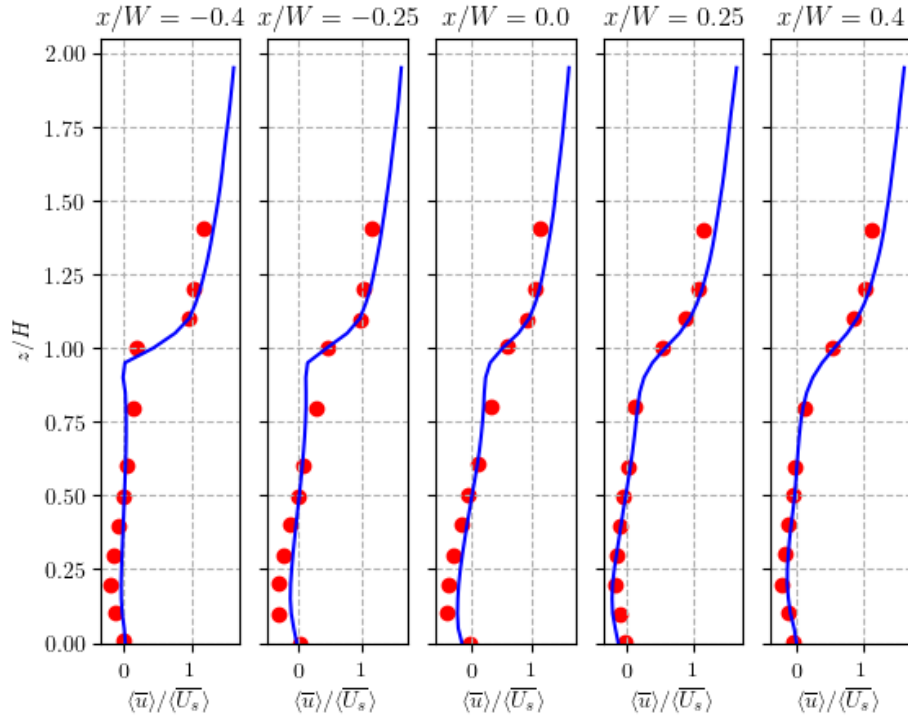
Figure 4. Vertical profiles of the normalised mean streamwise velocity, $\langle \overline{u} \rangle / \langle \overline{U_s} \rangle$, for the present LES and wind-tunnel measurements (Brown et al., 2001). $\langle \overline{U_s} \rangle$ is the average streamwise velocity within the shear layer ($1 \leq z/H \leq 1.5$). The LES results are plotted with blue lines, the wind-tunnel data with red circles.

where $\bar{N}$ is the time-averaged total number concentration (m^{-3}) and U_{ref} ($\mathrm{m\,s}^{-1}$) is the streamwise velocity at $2.5H$. In the
185 absence of aerosol dynamic processes (NOAD, left panels), the number concentration is essentially a passive scalar. For traffic emissions from the ground-level source (Fig. 6a), there are elevated concentrations within and around the vortex at the bottom leeward corner, as has been observed in many studies (for the related case of a line source see Pavageau and Schatzmann, 1999). For roadside cooking emissions from the windward side (Figs. 6b,c), pollutants recirculate around the corner before they can disperse through the rest of the canyon. Similar results for a pair of line sources were obtained by Huang et al. (2015); the fluid-
190 dynamical processes governing escape from the corner vortex are discussed by Duan et al. (2019), who analysed the initial-value problem rather than the forced one. Deep frying (NG-D) and boiling (NG-B) yield identical normalised concentrations in the absence of aerosol dynamic processes. In all cases, the concentration field reflects the combined influence of the mean flow (streamline geometry) and source location. Canyon-averaged number concentrations are summarised in Table 2.

The effect of aerosol dynamic processes (AD) is illustrated by the right panels. For traffic emissions, the spatial structure
195 of the number concentration field is almost identical (Fig. 6b) while the canyon-averaged and pedestrian-level concentrations decrease by around 2%. In their study of a neighbourhood in Cambridge, UK, K19 found that aerosol processes cause the number concentration to decrease by $\sim 10\%$. One possible explanation for this discrepancy is that the emission spectra differ:
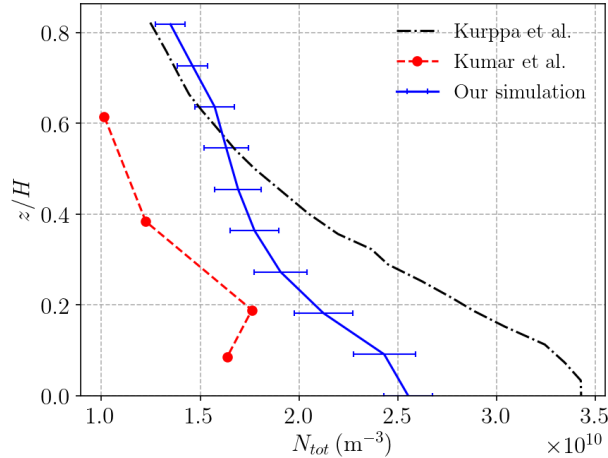
Figure 5. Vertical profiles of the aerosol number concentration within a street canyon in Cambridge, UK. The original in situ evening measurements (Kumar et al., 2008) are plotted in red. LES simulations using PALM-SALSA from K19 and the current study are plotted in black and blue, respectively. Error bars (standard deviations) for the current LES are plotted with horizontal lines.

Table 2. Canyon-averaged dimensionless concentrations, $\langle \bar{N} \rangle_C$, for the near-ground (Fig. 6) and column (Fig. 7) cooking emissions. The errors correspond to the spatial standard deviation; the relative change in the mean concentrations is also listed. Both the mean and standard deviation are time-averaged.

	Near-ground			Column		
	NOAD	AD	difference	NOAD	AD	difference
Boiling	144.4 ± 5.4	122.9 ± 3.5	-15%	193.1 ± 7.7	178.4 ± 5.8	-8%
Deep frying	144.4 ± 5.4	87.2 ± 1.4	-40%	193.1 ± 7.7	154.5 ± 2.5	-20%
Traffic	69.1 ± 2.4	67.7 ± 2.1	-2%	-	-	

the mean particle size is larger in the current study, i.e. 47.9 nm rather than 32.7 nm. This is significant because smaller particles (with a diameter less than 100 nm; K19) may have a larger deposition velocity, leading to enhanced deposition (see Sect. 3.3.2 for further discussion). For cooking emissions, the spatial structure of the concentration fields and the mean values change. With deep frying (Fig. 6d), the highest concentrations (shown in red) are confined to a smaller region in the windward corner and the isolines are strongly perturbed. With boiling (Fig. 6f), the highest concentrations are confined to a larger region and the isolines are deflected, though not as dramatically as for deep frying. The canyon-averaged concentrations decrease by 15% for boiling and 40% for deep frying. Since cooking, whether through boiling or deep frying, generates more small particles than does traffic (Fig. 3), the coagulation and dry deposition rates should be higher.

Of course the results will differ with other assumptions about the kitchen dimensions (Sect. 2.2.2). The sensitivity to the source flux is examined in Sect. 5.2.
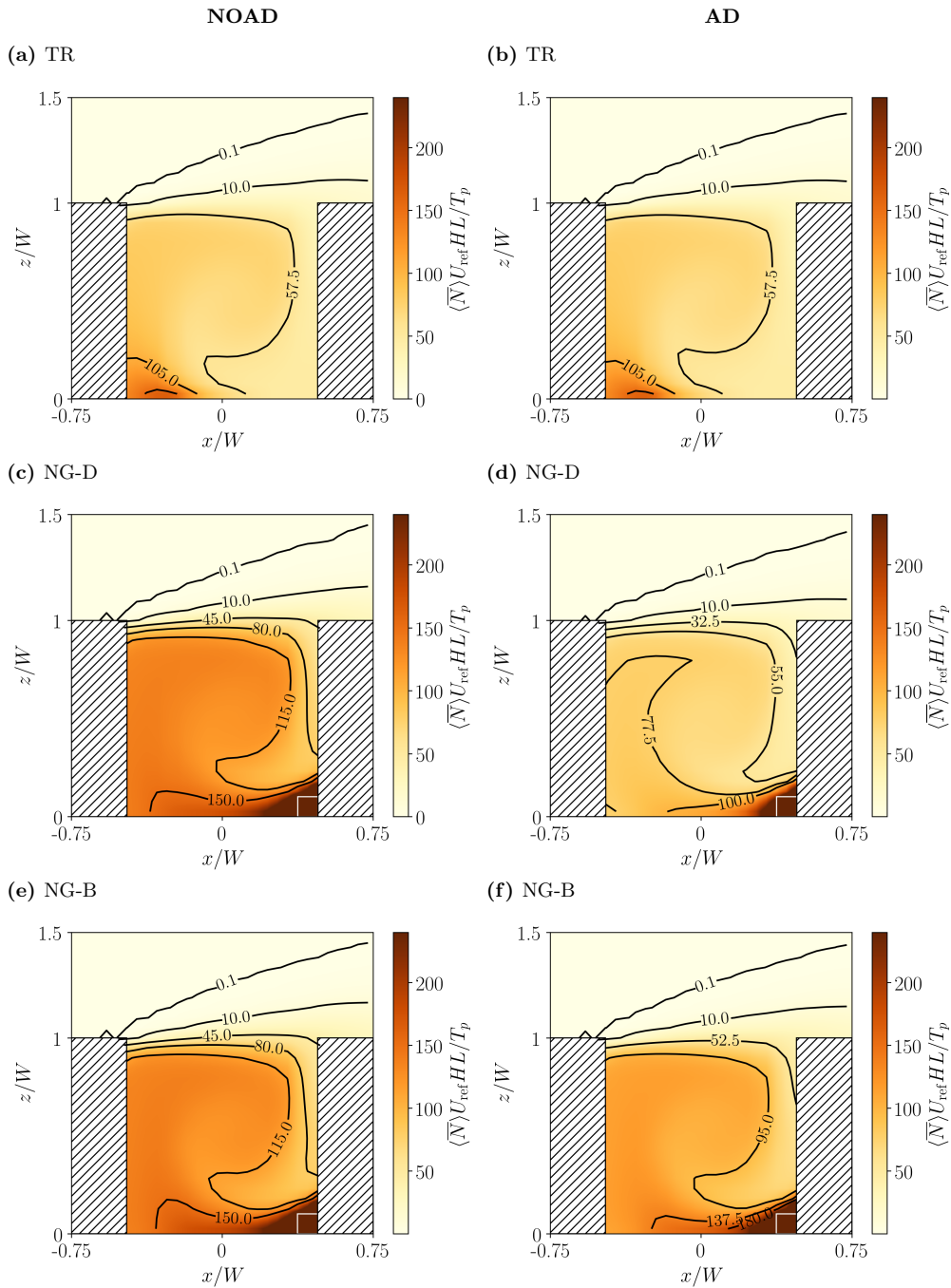
Figure 6. Normalised mean aerosol number concentration, $\langle \overline{N_*} \rangle$, for different emission scenarios: (a,b) traffic (Case TR); (c,d) near-ground, deep frying (Case NG-D); (e,f) near-ground, boiling (Case NG-B). Results without **(NOAD)** and with **(AD)** aerosol dynamic processes are shown at the left and right, respectively. The approximate position of the roadside restaurants is indicated by the white lines (which are shifted for clarity).

For reference, mass concentration fields are shown in Appendix D. In general, PM2.5 mass concentrations (i.e. for particles smaller than 2.5 μm in diameter) are higher for cooking emissions, especially for deep frying. Indeed the maximum concentration for NG-D reaches $200\,\mu g$ m^{-3} near the source region (Fig. D-1); possible reasons for these high values are given in Sect. 6. In agreement with the measurement campaign of Lee et al. (2015), the local contribution of cooking emissions exceeds that of traffic. However, the mass concentration shows much less sensitivity to the inclusion of aerosol processes.

3.2 Elevated kitchens
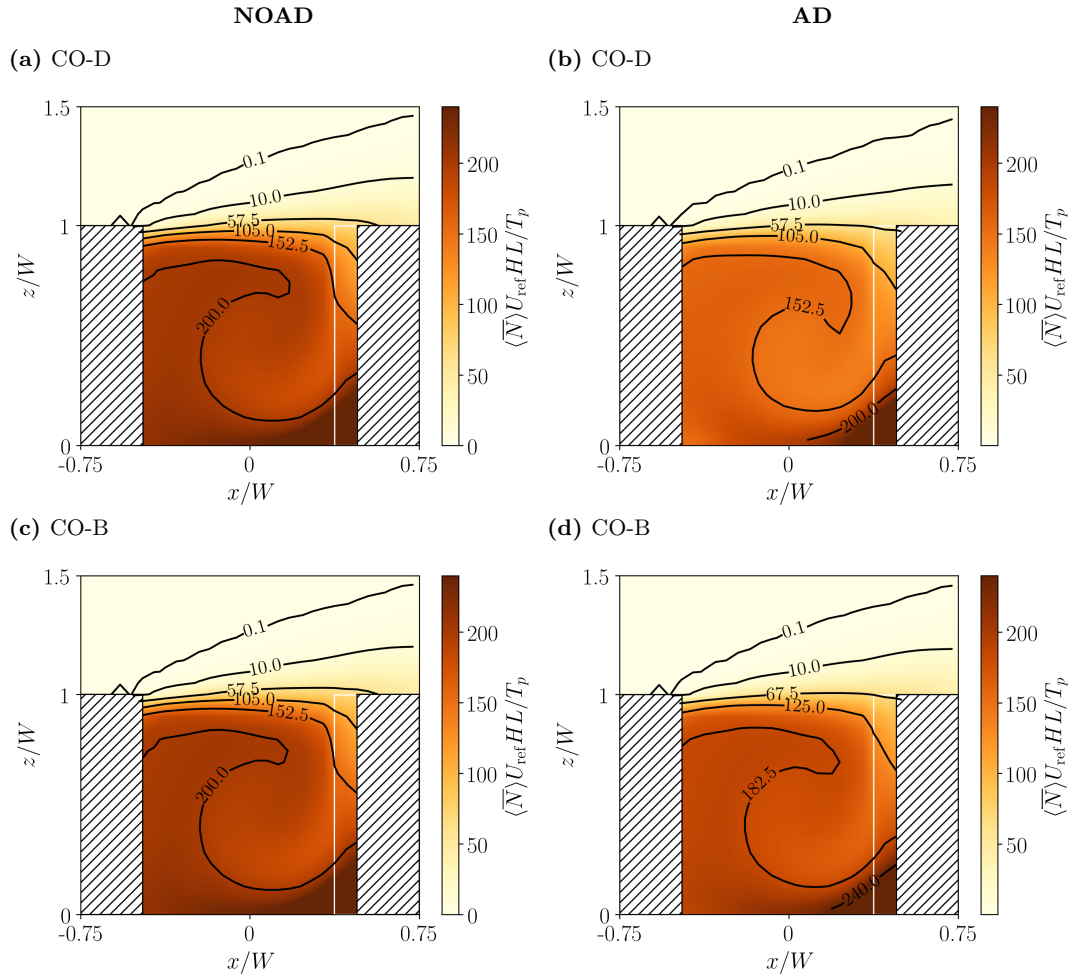
Figure 7. As in Fig. 6, but for column cooking emissions: (a,b) deep frying; (c,d) boiling.

Kitchens may not be located at the roadside. This section considers continuous emissions along a column extending from the bottom to top of a building, as well as isolated kitchens on different levels.

The qualitative effect of column cooking emissions resembles the near-ground emissions. For both deep frying and boiling, the familiar pattern of very high concentrations in the bottom leeward corner and lower concentrations aloft is maintained (Fig. 7); however, the concentrations increase in the interior. Averaged over the canyon, the spatial mean and standard deviation increase for column emissions (Table 2), but the sensitivity to aerosol processes weakens: the difference between NOAD and AD is 8% and 20% for boiling and deep frying, respectively. If the number concentration depended linearly on particle emissions, the nondimensionalisation would remove the dependence on the total particle flux, T_p; nonlinear effects are discussed in Sect. 5.1.

The influence of the source height is stronger for the isolated kitchens. Normalised mean aerosol number concentrations for I-B-z_0 are shown in Fig. 8. Although trapping of particles within the vortex at the bottom leeward corner is less evident as the source height is increased from $z_0/H = 0.05$ to $z_0/H = 0.95$ (Figs. 8a-c), as the contrast with the interior weakens, but emission from the elevated sources actually increases the canyon-averaged concentrations. The vertical profiles (Fig. 8d) show that concentrations are maximised for $z_0/H = 0.5$, which is consistent with elevated concentrations around the central canyon vortex (Duan et al., 2019). Canyon averages show that the effect of the aerosol processes is greatest for ground-level emission, $z_0/H = 0.05$ (Table 3). The results for I-D-z_0 are similar (see Supplementary Material, Fig. S-1).

Table 3. As in Table 2, but for deep-frying and boiling emissions from isolated kitchens.

	NOAD	AD	difference
I-B-0.05	219.3 ± 7.2	200.0 ± 5.5	-9%
I-B-0.50	289.9 ± 10.8	276.2 ± 8.7	-5%
I-B-0.95	242.5 ± 13.8	231.4 ± 11.8	-5%
I-D-0.05	219.3 ± 7.2	181.3 ± 3.0	-17%
I-D-0.50	289.9 ± 10.8	264.4 ± 4.7	-9%
I-D-0.95	242.5 ± 13.8	232.4 ± 4.3	-4%

3.3 Comparison of aerosol dynamic processes

The effect of the individual aerosol processes is assessed by analysing separate SALSA configurations in which condensation, coagulation, deposition, or all three processes acting simultaneously, are enabled. As in K19, the relative difference,

$$RD_i = \frac{\langle \overline{N_{NOAD}} \rangle - \langle \overline{N_i} \rangle}{\langle \overline{N_{NOAD}} \rangle}, \tag{2}$$

is defined from the mean concentrations with aerosol processes, $\langle \overline{N_i} \rangle$, and without them, $\langle \overline{N_{NOAD}} \rangle$. In the former case, $i \in \{\text{COND}, \text{COAG}, \text{DEPO}, \text{ALL}\}$ labels the different SALSA configurations. The subscript is dropped when there is no risk of confusion. For brevity, not all of the emission scenarios listed in Table 1 are analysed here. Results for boiling may be found in Supplementary Material, Fig. S-2 and Fig. S-3).

(a) I-B-0.05   **(b)** I-B-0.50

(c) I-B-0.95   **(d)** Vertical profiles
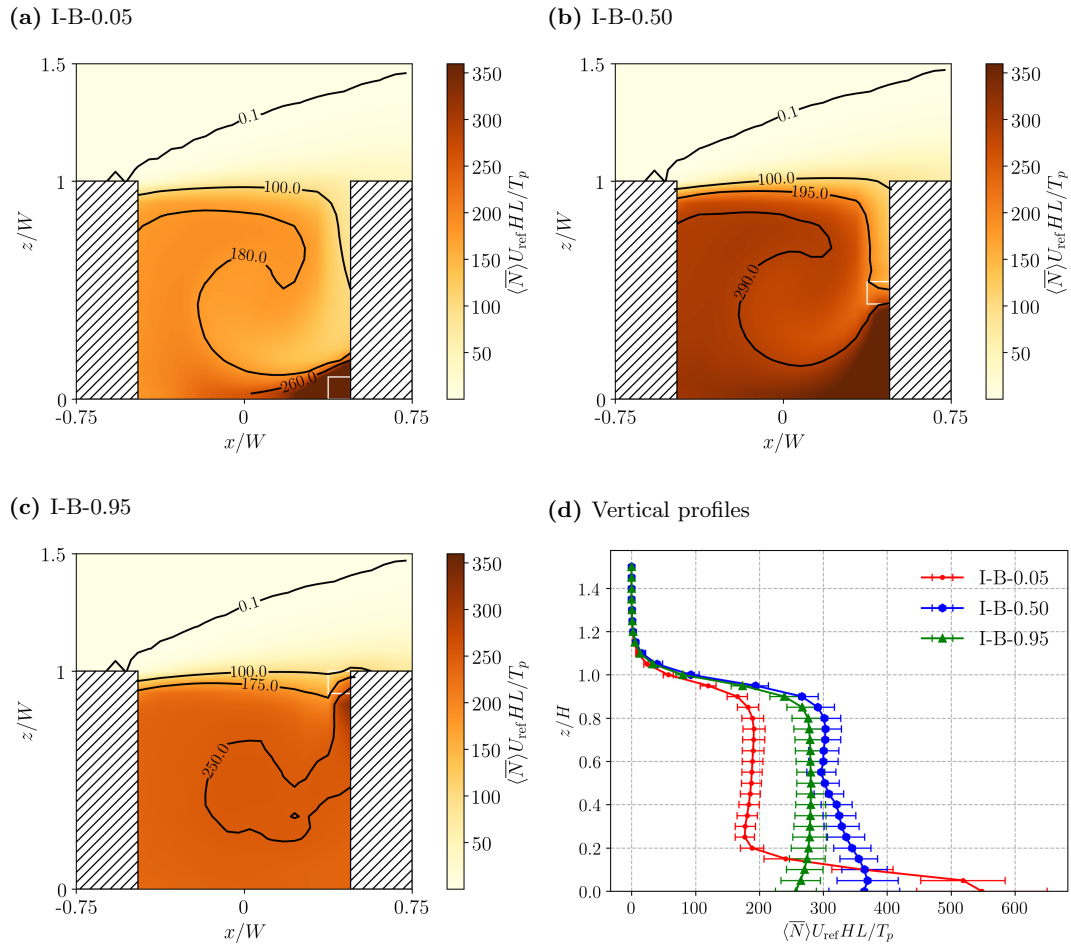
Figure 8. As in Fig. 6, but for isolated kitchens and boiling. The kitchens are located at (a) $z/H = 0.05$; (b) $z/H = 0.5$; (c) $z/H = 0.95$. Mean vertical profiles are plotted in (d).

3.3.1 Traffic emissions

Figure 9 compares the effects of the different aerosol processes for traffic emissions. Vertical profiles of the mean number
240   concentration have nearly identical shapes for the different configurations (Fig. 9a). The lowest concentrations are obtained for deposition only. On account of nonlinearity, the effects do not add linearly. By contrast with K19, who considered a domain with uneven building heights, the relative difference shows minimal variation with height (Fig. 9b). Condensation has a negligible effect on the aerosol number concentration, which is consistent with the notion that it primarily serves to increase the volume of particles (Seinfeld and Pandis, 2016). The effects of deposition and coagulation are approximately constant away from the
245   bottom boundary. For $z/H > 0.2$, $RD \sim 4.5\%$ for deposition and $\sim 0.4\%$ for coagulation. The estimate of RD_{DEPO} is low compared to K19, who obtained $RD_{DEPO} \sim 15\%$ using a different emission spectrum, non-zero background concentration

and realistic urban topography. Nonetheless, deposition remains the most important process for traffic emissions, in agreement with the timescale analysis of Ketzel and Berkowicz (2004).
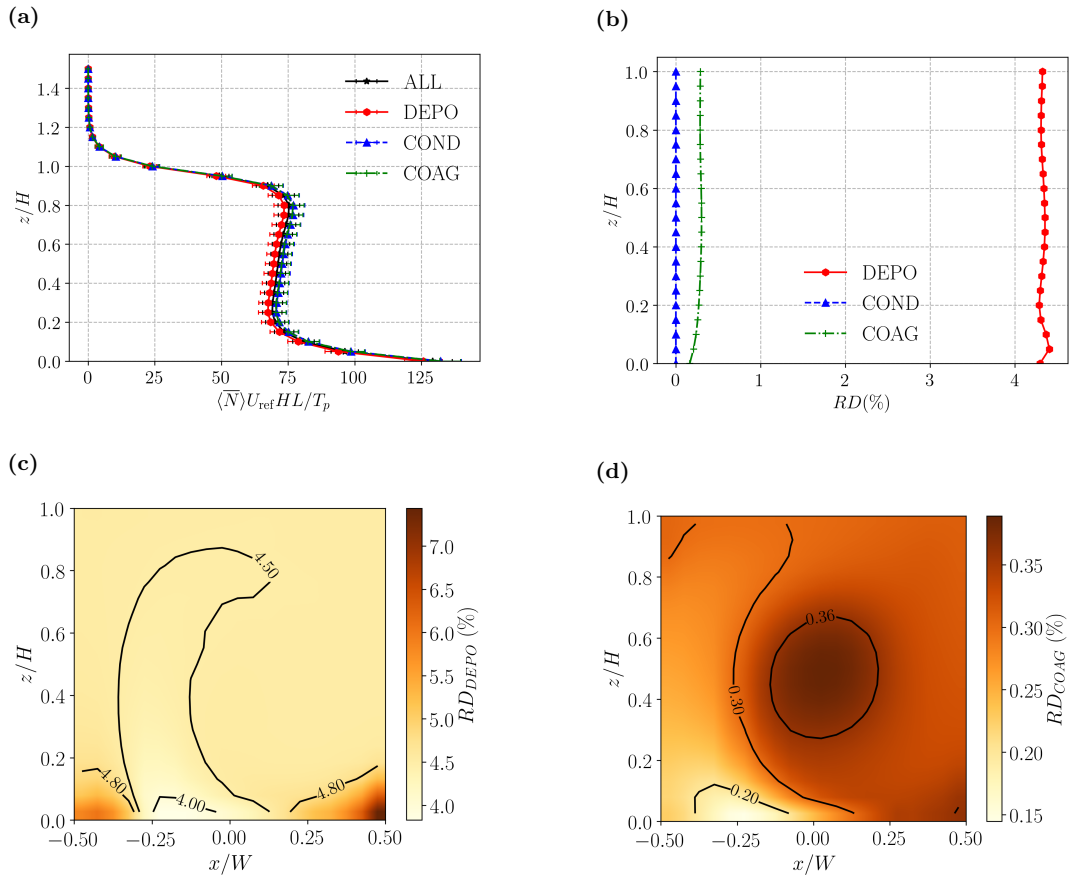
Figure 9. Effect of different aerosol processes for Case TR. Mean vertical profiles of **(a)** mean aerosol number concentration; **(b)** relative difference with respect to a simulation without aerosol dynamic processes (NOAD). Spanwise-averaged relative difference fields for **(c)** deposition; **(d)** coagulation. The lines correspond to different SALSA configurations (DEPO – deposition only; COND – condensation only; COAG – coagulation only; ALL – deposition, condensation and coagulation).

We now consider the spatial structure of the two most important processes. For deposition (Fig. 9c), RD is maximised in the 250   bottom corners. Values are lower away from the corners, especially near the centreline, $x/W = 0$. For coagulation (Fig. 9d), by contrast, the pattern is rather different: RD is maximised within the bottom windward vortex and the central canyon vortex. Roughly speaking, the effects of deposition are fairly small outside the bottom corner vortices, while those of coagulation tend to increase away from the source centred at $x/W = 0$. The increase follows the orientation of the mean circulation (cf. Fig. 2a).
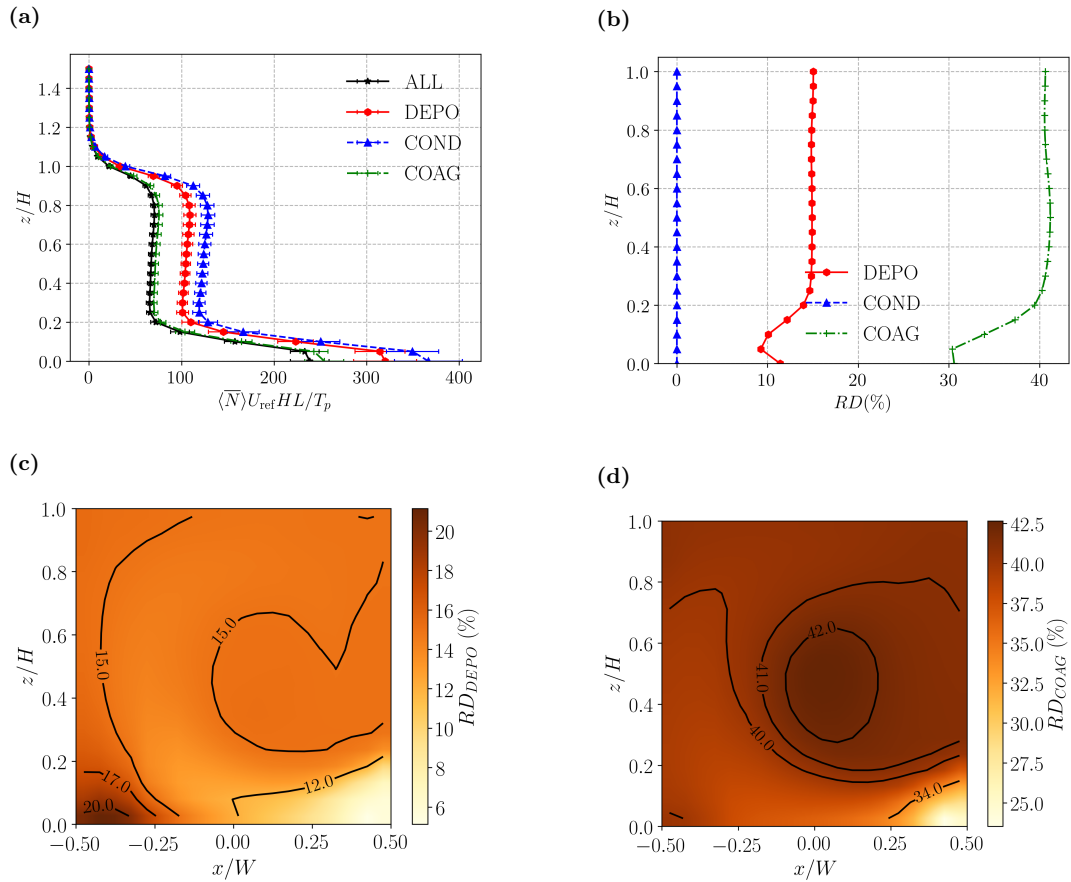
Figure 10. As in Fig. 9, but for Case NG-D.

3.3.2 Near-ground cooking emissions

The effects of the different aerosol processes for near-ground deep frying are compared in Fig. 10. Compared with traffic emissions, the effects of coagulation are much more important: the vertical profiles for COAG and ALL nearly coincide (Fig. 10a) and RD_{COAG} reaches a maximum of around 40% (Fig. 10b), which is around 400 times higher than that for traffic emissions. RD_{DEPO} also increases significantly. There are several reasons for these differences. First, coagulation occurs more efficiently for particles with $D_p < 50$ nm (Kokkola et al., 2008). Such particles are favoured by the emission spectrum (93% of the particles generated by deep frying fall in this category, but just 58% for traffic; Fig. 3). Second, the efficiency of Brownian diffusion increases for smaller particles, leading to higher deposition velocities and enhanced deposition (Zhang et al., 2001; Kurppa et al., 2019). Above $z/H \sim 0.2$, which lies above the corner vortices in Fig. 2, the RD profiles are nearly independent of height.

The spatial structure of the RD fields also changes. For deposition (Fig. 10c), RD is maximised in the bottom leeward corner, while the lowest values are found in the bottom windward corner. (RD gives an exaggerated impression of the absolute difference between the corners as the total number concentration for NOAD is approximately 50% higher in the windward corner.) For coagulation (Fig. 10d), the lowest values are no longer found around the source centred at $x/W = 0$, as is the case for traffic (Fig. 9d), but rather around the roadside kitchens on the windward wall. Once again, there is indication that the relative importance of coagulation increases away from the source following the sense of the mean circulation. The largest RD values are found near the centre.

Qualitatively similar results are obtained for Case NG-B (Supplementary Material, Fig. S-2). While number concentrations and RD values are lower (cf. Table 2), the structure of the RD fields is largely unchanged from Fig. 10.

3.3.3 Column cooking emissions

The effects of the different aerosol processes for column deep frying are compared in Fig. 11. Although the emission spectrum is unchanged from Case NG-D (Fig. 10), both RD_{DEPO} and especially RD_{COAG} decrease (Fig. 11b). This change cannot be directly attributed to the increase in the canyon-averaged number concentration (Table 2). Everything else being the same, the deposition rate should scale linearly with $\bar{N}$ (Sect. A.1), while the coagulation should scale quadratically (Sect. A.2). Given the nondimensionalisation and the increase in $\bar{N}$, one would naively expect RD_{DEPO} to be approximately unchanged and RD_{COAG} to increase. Evidently the change in the source configuration, rather than the associated increase in number concentration, is of primary importance. The spatial distribution provides partial insight into this. Analogously to NG-D, RD_{DEPO} and RD_{COAG} have relatively low values along the windward wall (Figs. 11c,d); however, the column source covers a larger area and a plume-like structure (i.e. the tongue of low RD values between the canyon centre and the windward wall) develops away from it. Results for CO-B are qualitatively similar (Supplementary Material, Fig. S-3).

3.4 Aerosol number distributions

Aerosol size distributions for ground-level traffic and near-ground cooking are compared in Fig. 12 for different emission scenarios and SALSA configurations. The statistics are evaluated over the entire canyon. Deviations with respect to NOAD reflect the influence of aerosol processes. For Case TR (Fig. 12a), deposition decreases the number of particles in each size bin for $D_p < 50$ nm, but has minimal effect for larger particles. The shape is not exactly preserved because deposition is size-dependent (cf. Sect. A.1). The size spectra for COAG and NOAD are almost identical. The effect of coagulation on the size spectra is more obvious for cooking emissions. For Case NG-D (Fig. 12b), the COAG and ALL spectra are nearly identical; the DEPO concentrations are higher at small scales, $D_p < 40$ nm. For Case NG-B (Fig. 12c), the pattern is similar. The effects of COAG are largest for small particles on account of the emission spectra and the increase in coagulation efficiency for smaller particles.

Similar results are obtained for column emissions. For Case CO-D (Fig. 12d), differences with respect to NOAD are smaller, in agreement with the canyon-averaged concentrations, but compared to NG-D, the range over which coagulation is strongest
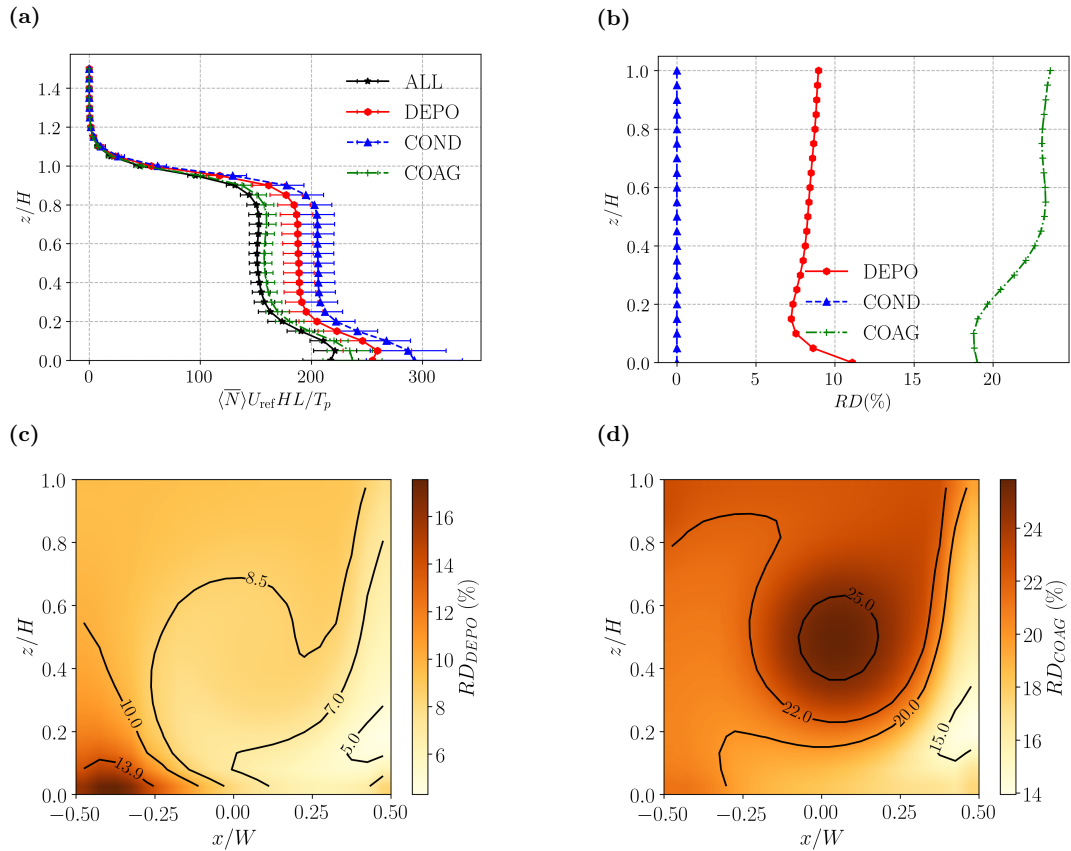
Figure 11. As in Fig. 9, but for Case CO-D.

narrows to $D_p \leq 30$ nm. For Case CO-B (Fig. 12e), coagulation leads to decreased concentrations for small particles ($D_p <$ 20 nm), as with NG-B.

The uncertainty in the estimate of the time-averaged size distributions is indicated with the (temporal) standard error. Errors are much smaller for the deep-frying cases, NG-D and CO-D. A plausible explanation is that temporal intermittency is greater for cases in which deposition plays a more important role, namely TR, NG-B and CO-B, because deposition only occurs near surfaces and is maximised inside the corner vortices. Coagulation, by contrast, occurs everywhere.

4 Analysis of the aerosol processes

4.1 Characteristic timescales

The differences between the aerosol processes can be understood by referring to the characteristic timescales (Fig. 13). For concreteness, we focus on NG-D. The deposition timescale is derived from the deposition velocity, eq. (A1a), which is
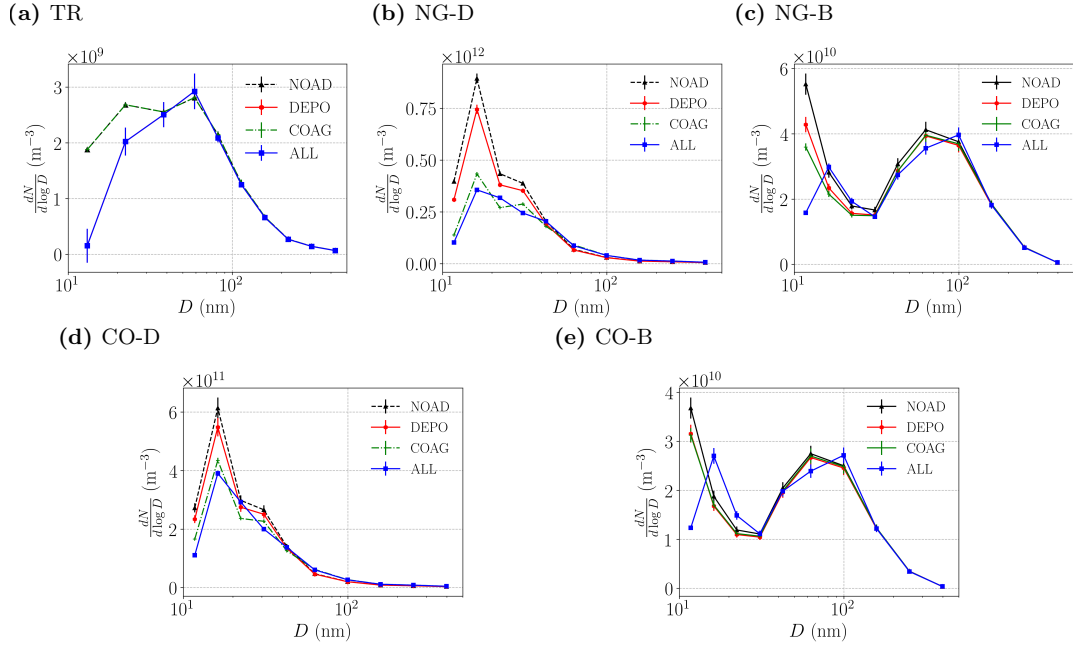
Figure 12. Canyon-averaged aerosol number size distributions for different emission scenarios: (a) traffic; (b) near-ground deep frying; (c) near-ground boiling; (d) column deep frying; (e) column boiling. Each line corresponds to a different set of aerosol processes (see Fig. 9 for definitions). The standard error (obtained from the temporal standard deviation) is denoted by the error bars.

$O(10^{-2})\,\mathrm{m\,s^{-1}}$ Hence the deposition timescale for the smallest resolved scale, $\tau_{depo} = \Delta/v_d \sim 150$ s, while for the corner vortices, $\tau_{depo} = O(500)$ s. Following Ketzel and Berkowicz (2004), the coagulation timescale,

$$\tau_{coag} = N/\frac{\partial N}{\partial t}\big|_{coag}, \tag{3}$$

may be diagnosed from the evolution equation,

$$\frac{\partial N}{\partial t}\big|_{coag} = \frac{1}{2}\sum_{j=1}^{k-1}\beta_{k-j,j}n_{k-j}n_j - \sum_{j=1}^{\infty}\beta_{k,j}n_k n_j \tag{4}$$

where β_{ij} is the coagulation kernel. Although this neglects the actual time discretisation (cf. Sect. A.2), the error should be negligible so long as $\Delta t \ll \tau_{coag}$. Using the same β_{ij} as SALSA and $\bar{n}_i$, the time-averaged number concentrations, $\tau_{coag} \sim 50000 - 500000$ s for NG-D (Fig. 13b). However, this estimate is somewhat misleading because τ_{coag} is not constant. From integration of eq. (4), the total number concentration actually decreases from its initial value (i.e. the time-averaged n_i) by a factor of e after ~ 1000 s (not shown).

Given these estimates for τ_{depo} and τ_{coag}, several predictions about deposition and coagulation can be made. Deposition will preferentially occur where particles can remain close to solid surfaces for an extended duration; the corner vortices are good candidates because particles may be brought near the walls as they recirculate. This is consistent with RD_{DEPO} (Fig. 10b).
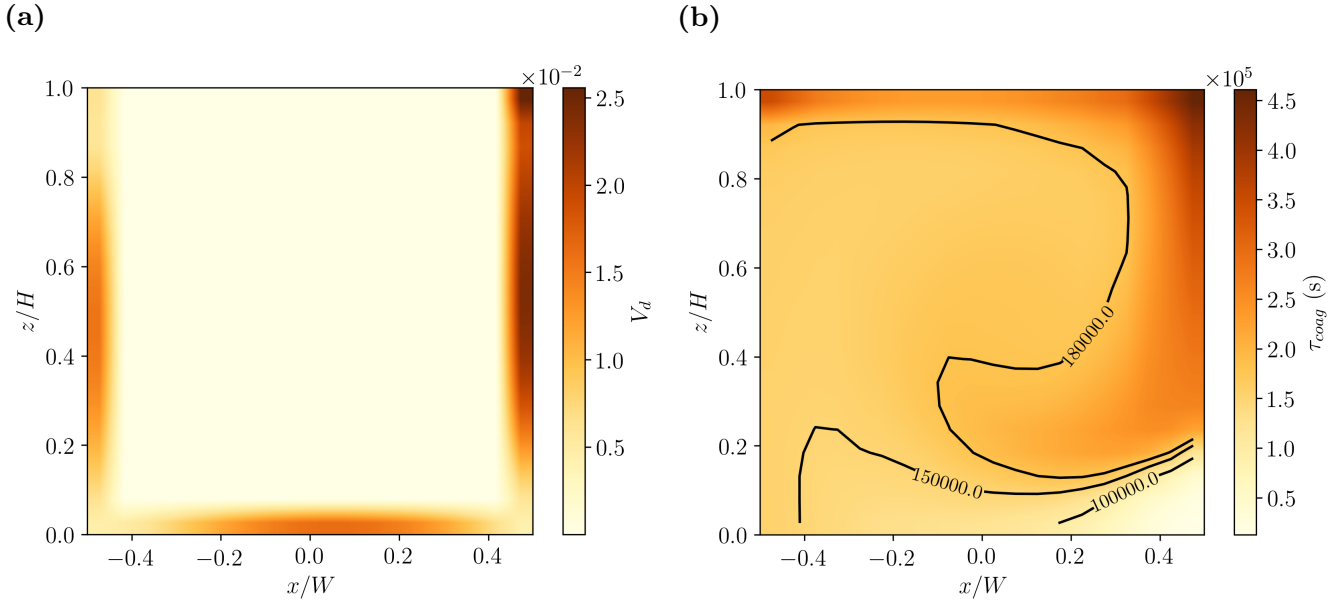
Figure 13. Comparison of characteristic timescales for NG-D. (a) v_d (or Δ/τ_d); (b) τ_{coag}.

Away from the walls, τ_{depo} is not uniform in the interior because particles are mixed with ambient fluid. The aerosol timescales
320 may be compared to the mean circulation timescale, i.e. $T_c \equiv 2(H/W + U/W) = 382$ s, where U and W are characteristic streamwise and vertical speeds, which yields a good estimate of the mean residence time of pollutants within the canyon (Lo and Ngan, 2017). Since $\tau_{depo} \lesssim T_c$, deposition is partially but not completely independent of the mean canyon motion; thus deposition does not occur immediately. By contrast, $\tau_{coag} \gg T_c$ so that coagulation within the canyon proceeds while particles are being advected and mixed. One therefore expects the structure of RD_{COAG} to resemble that of the steady passive scalar
325 field (compare Figs. 6c and 9d). More precisely, RD_{COAG} should be correlated with the age of fluid parcels or the time elapsed between the release of a particle at the source and its arrival at a receptor point. Physically, RD_{COAG} increases away from the source (i.e. as the age increases) because there is more time for coagulation to occur.

Similar considerations apply to other emission scenarios. For NG-B, v_d is comparable $\tau_{coag} \sim 100000 - 500000$ s (with an e-folding time of 7000 s). The implication is that the spatial structure of RD_{DEPO} and RD_{COAG} should be largely unchanged.
330 Deposition is strongly affected by the emission spectrum (cf. Fig. 12), but it should continue to be maximised in the same places for identical flow and source location. Coagulation is much slower compared to NG-D and RD_{COAG} reduced, but the basic pattern should be unchanged so long as coagulation is a relatively slow process governed by the age along fluid trajectories. These predictions are consistent with Supplementary Material, Fig. S-2. For CO-B, v_d and τ_{coag} change little from NG-B (by 3.1% and 4.0%). As before, one expects deposition to increase within the corner vortices, though the effect on RD_{DEPO}
335 should be less noticeable within the windward vortex, where concentrations are higher around the source (Fig. 7c). Coagulation should decrease for CO-B on account of the shorter mean ages associated with elevated source locations (see Sect. 4.2).

4.2 Mean tracer age
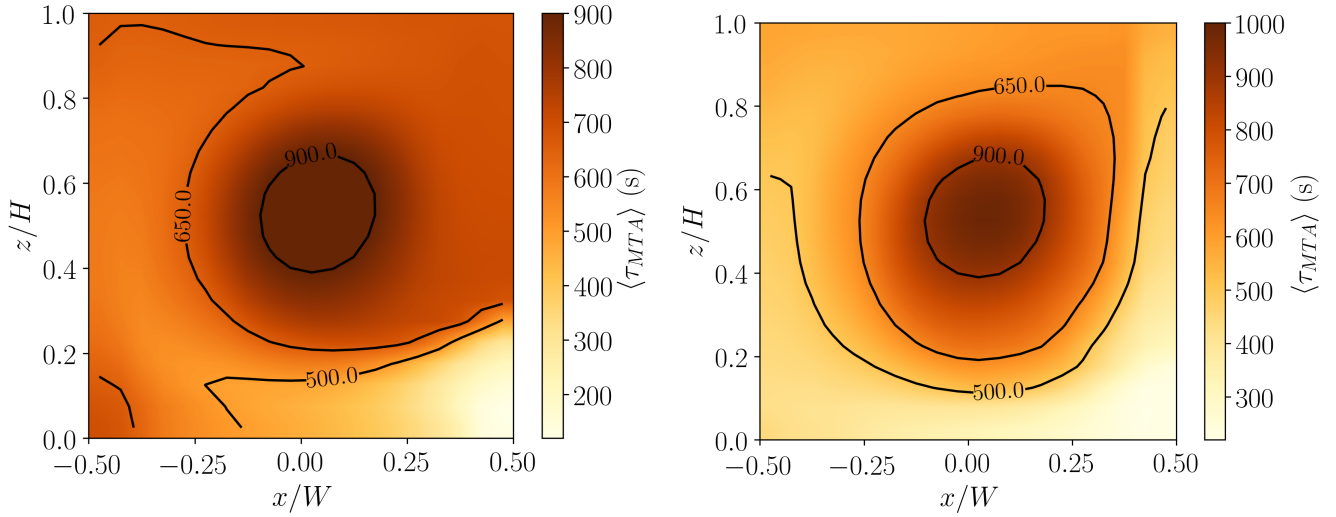
Figure 14. Spanwise-averaged MTA for (a) near-ground; (b) column source. The canyon-averaged MTAs are similar (652 s for the NG source and 599 s for the CO source); however, the spatial structures are noticeably different.

To test these predictions, the age may be calculated by tracking fluid parcels. The mean tracer age (MTA; Lo and Ngan, 2015) characterises the average time elapsed between the release of a pollutant at the source and its arrival at the receptor. This is a more appropriate dynamical timescale for coagulation. Following the procedure reviewed in Appendix E, the MTA is calculated for a near-ground source (Fig. 14a). The MTA is lowest near the source at the bottom windward corner and increases towards the centre of the domain, where there are very high values. This pattern is seen most clearly in RD_{COAG} (Fig. 10d) and to a lesser extent, RD_{ALL} (not shown). Linear correlation coefficients between the MTA and the relative difference for NG-D confirm that coagulation is strongly dependent on the age (Table 4). The correlation is weaker for deposition because the MTA is not maximised around the leeward corner. The magnitude of the correlation with RD_{DEPO} is comparable to that with the total number concentration (not shown), which tends to decrease away from the source. For a column source (Fig. 14b), the correlation between the MTA and the relative differences is comparable.

MTA	RD_{COAG}	RD_{DEPO}	RD_{ALL}
NG-D	0.90	0.57	0.77
CO-B	0.86	-0.15	0.16

Table 4. Linear correlations between the relative differences and the MTAs for NG-D and CO-B.

The preceding results imply that resolving the transient dynamics is potentially important for accurate simulation of aerosol dynamical processes. Since coagulation is nonlinear in the concentration and the concentration evolves between the source and receptor, approximating the coagulation term with a time average will introduce errors. These errors could be significant when coagulation is strong, such as is the case for cooking emissions.

The dynamical and aerosol timescales are summarised in Table 5. In all cases, $\tau_{depo}/T_c \lesssim 1$ and $\tau_{coag}/MTA \gg 1$.

Table 5. Dynamical and aerosol timescales for different emission scenarios.

Source location	T_c (s)	MTA (s)	Emission scenario	τ_{depo} (s)	τ_{coag} (s)
TR	382	584	TR	150	1.1×10^7
NG	382	652	NG-D	150	1.8×10^5
			NG-B	150	1.2×10^6
CO	382	599	CO-D	150	2.2×10^5
			CO-B	150	1.8×10^6

5 Sensitivity tests

5.1 Background concentrations

The calculations described in Sect. 3 neglect background concentrations, i.e. $N_b = 0$. Although N_b is fixed, the background is still involved in aerosol processes. To assess the effect of the background on the aerosol processes, several cases with $N_b > 0$ are considered.

1. Idealised background spectrum. Here it is assumed that the background spectrum is identical to the emission spectrum. Using a single emission scenario, NG-B, two cases are considered: (i) light pollution, $N_b = 0.1N_0$; (ii) heavy pollution, $N_b = 0.4N_0$, where N_0 is the mean canyon-averaged number concentration for $N_b = 0$. These values are arbitrary; however, the increase in N_b is meant to capture the contrast between normal conditions and a severe pollution episode.

2. Realistic urban background spectrum. Here NG-B is applied to the background spectrum from a real urban measurement (Fig. 15d). The measurement was taken in Tsuen Wan, Hong Kong (see Appendix G for details). The measured spectrum resembles the emission spectrum for traffic (Fig. 3). The measurements suggest $N_b = 0.5N_0$.

Spatially uniform, constant background concentrations are prescribed over the entire computational domain. The effect of the background is assessed by calculating RD_{ALL} for different N_b. Note that the background is allowed to interact with the emissions through heterogeneous coagulation. For the idealised cases, RD_{ALL} decreases as the background concentration is increased to $N_b = 0.1N_0$ and $N_b = 0.4N_0$ (Table 6); for the realistic case, RD_{ALL} decreases by up to 37% from its value for $N_b = 0$. Nevertheless, the actual impact is smaller than it may appear on first glance. In the absence of any additional
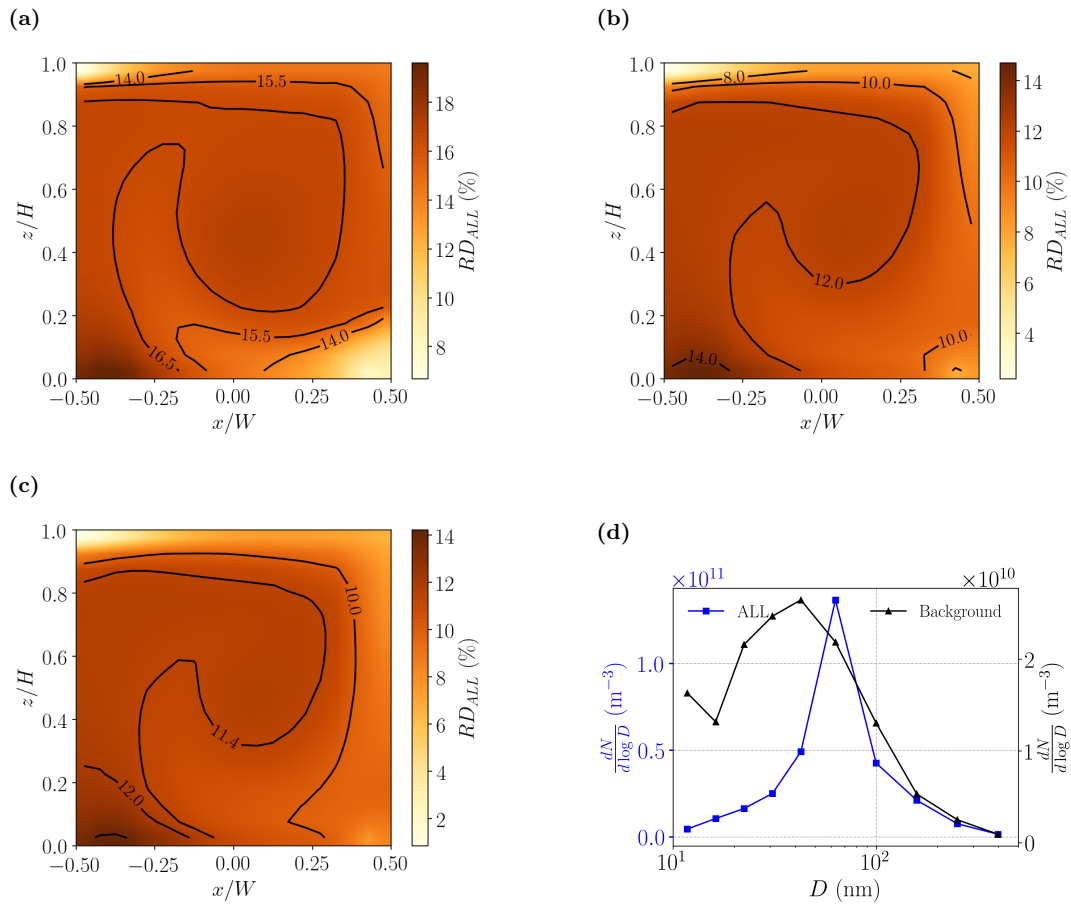
Figure 15. Spanwise-averaged relative difference fields of aerosol dynamical processes (ALL). (a) light pollution; (b) heavy pollution; (c) realistic case; (d) aersol number size distributions for background concentration (black line) and total concentration (blue line).

Baseline	Idealised		Realistic
$N_b = 0$	$N_b = 0.1N_0$	$N_b = 0.4N_0$	$N_b = 0.5N_0$
16.96%	16.03%	11.41%	10.69%

Table 6. Canyon-averaged RD_{ALL} for $\overline{\text{NG-B}}$ and different background cases. Note that the baseline concentration ($N_b = 0$) is identical for idealised and realistic cases.

370 aerosol processes, e.g. if the background were completely inert, RD_{ALL} would also decrease from the accompanying increase in the total number concentration, N: for $N_b = 0.1N_0, 0.4N_0$ and $0.5N_0$, the decreases would be 15.4%, 12.1% and 11.3%, respectively. On account of aerosol processes involving the background only or the background and emissions, the values in Table 6 depart from the crude linear scaling, but the deviations are small, i.e. $\sim 5\%$. The qualitative similarity of the RD_{ALL}

fields (Figs. 15a-c) suggests that the physical mechanisms described in Sec. 4 are robust. This is true even though the simulated size distribution shifts towards large particles when the realistic background spectrum is used (Fig. 15d).

The effect of the background on N is relatively small because N_b is fixed. Hence aerosol processes involving the background do not change N directly: the background affects N only indirectly through the emissions. For example, coagulation between the background and emissions will change the size distribution of the nominal emissions (i.e. the "perturbation" or $N - N_b$), which will in turn affect the deposition and coagulation rates. This is clearly a nonlinear process.

5.2 Source flux

The dependence on the source flux is usually ignored in studies of pollutant dispersion. For a passive scalar emitted by a uniform source, the concentration scales linearly with the source flux and this dependence can be removed by the nondimensionalisation, eq. (1). For aerosols, however, this is no longer true because coagulation depends nonlinearly on the number concentration. This is potentially important because cooking emissions are not constant with time. Here we assess the sensitivity to the source flux Q for Case CO-B. Letting the original source flux be denoted by Q_0, we now consider $Q = \alpha Q_0$ for $\alpha \in [0.1, 10]$.

The effect on the different aerosol processes is illustrated by vertical profiles of RD_i. For $Q = 0.1Q_0$ (Fig. 16a) and $Q = 10Q_0$ (Fig. 16b), condensation is negligibly small. Deposition also shows weak sensitivity to the source flux as $RD_{DEPO} \sim 8\%$ despite the hundredfold increase in Q. However, coagulation shows strong sensitivity to Q_0: it is small for $Q = 0.1Q_0$ ($RD_{COAG} \sim 0.5\%$) but of major importance for $Q = 10Q_0$ ($RD_{COAG} \sim 25\%$). Examining RD_{COAG} separately (Fig. 16c), the sensitivity is fairly weak for $Q/Q_0 \leq 1$.

The preceding results may be explained as follows. The dry deposition flux for size bin i is linearly proportional to the concentration, i.e. $F_{d,i} = -v_d n_i$, where v_d is the deposition velocity (Seinfeld and Pandis, 2016). The number concentration is directly proportional to Q but this dependence disappears from RD_{DEPO} after the nondimensionalisation. The corresponding coagulation flux (i.e. the contribution of coagulation to the time evolution of n_i) is quadratic in n_i, implying that coagulation should depend sensitively on the source flux. This is partially confirmed by vertical profiles of the normalised concentration, N/Q (Fig. 16d), which suggest a nonlinear dependence on Q for $Q/Q_0 > 1$.

6 Discussion

This study has focused on an idealised flow and a small number of representative emission scenarios in order to highlight the basic processes governing the dynamics of cooking-generated urban aerosols. We now discuss how the results may extend to more realistic cases.

The emission scenarios defined in Table 1 are arbitrary. Obviously other kitchens dimensions or locations could be chosen, but the results presented here should serve as a starting point for future studies of specific urban environments. The sensitivity to the source flux cannot be strictly neglected, but at least for deviations of $\sim 50\%$ from the baseline value, the effect is modest (Fig. 16). The qualitative response to the source location can be estimated from the behaviour for a passive scalar as the inclusion of aerosol processes has little effect on spatial structure of the number concentration fields (e.g. Fig. 1b).
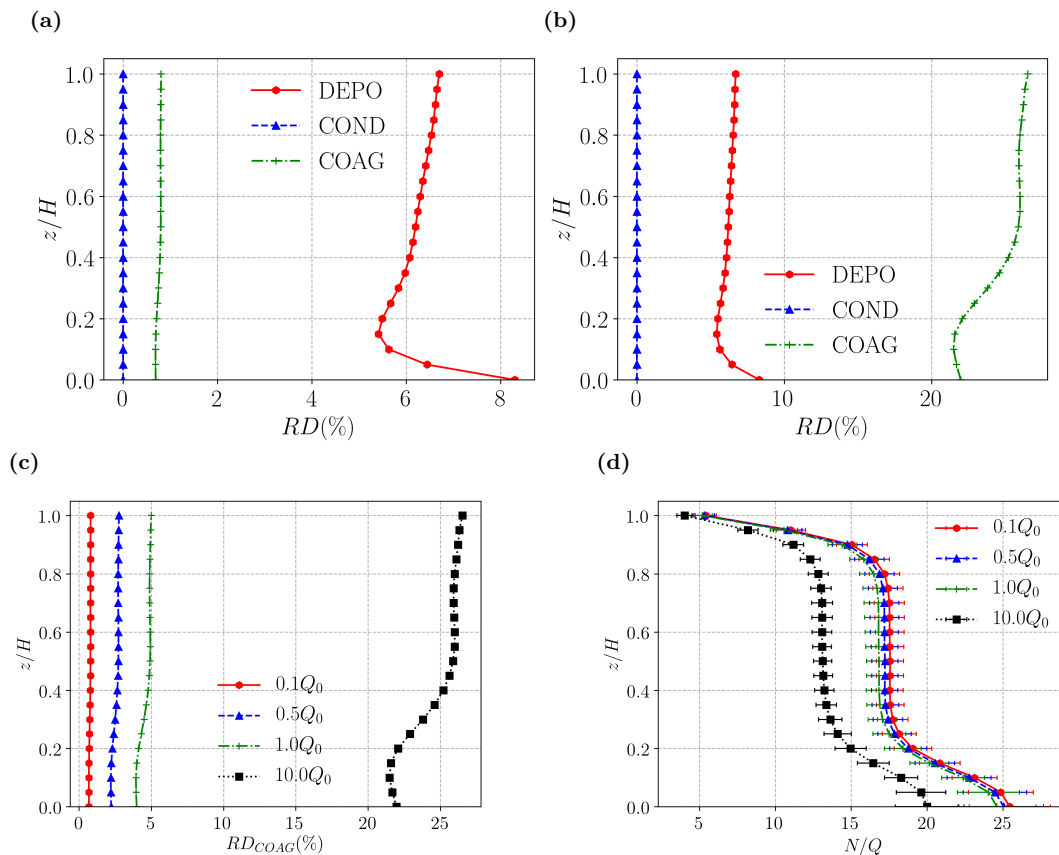
Figure 16. Comparison of aerosol processes and source fluxes, Q, for Case CO-B, The top panels compare vertical profiles of RD_i at fixed Q, the bottom panels compare the effect of different Q on coagulation. (a) $Q = 0.1Q_0$; (b) $Q = 10Q_0$; (c) RD_{COAG}; (d) normalised number concentration, N/Q.

Although the results inevitably depend on the emission spectrum — mean concentrations for boiling and deep frying differ by $\sim 30\%$ for near-ground emissions and $\sim 15\%$ for column emissions (Table 2) — there is no evidence for strong sensitivity. Test calculations in which the emission spectrum for NG-B is scaled by a factor of 2 or 0.5 show limited sensitivity. For example, the vertical profiles show a nearly identical shape with mean concentrations differing by less than 5% with respect to the default emission spectrum (Supplementary Material, Fig. S-4). Furthermore, the spatial structure of the relative difference fields is almost identical (Supplementary Material, Fig. S-5).

Flow over a unit-aspect-ratio street canyon has been a benchmark case for examining urban air quality chemistry (Zhong et al., 2015) because it captures the effects of decreased ventilation, or equivalently, a finite residence time for chemical reaction (Harrison, 2018). The analysis of Sect. 4 implies that the spatial structure of deposition and coagulation are determined primarily by two factors: the streamline geometry or mean circulation and the ratio of the aerosol and dynamical timescales. Deposition is promoted when particles are brought into repeated contact with solid surfaces, such as occurs within corner

vortices. Coagulation requires the ageing of pollutants, which occurs along fluid trajectories in the outdoor environment. Hence the nature of the aerosol dynamics for a given emission spectrum should depend on the ratio of the aerosol timescales to the dynamical timescales, at least for relatively small perturbations in which the streamline geometry is maintained. This is a variant of the argument that the nature of urban gas phase chemistry is strongly influenced by the ratio of the chemical timescale to the residence time (Harrison, 2018).

With other emission scenarios or flows, quantitative differences are unavoidable, but qualitative differences in the aerosol dynamics are not expected in most cases. For cooking emissions, the coagulation timescale is much longer than the relevant dynamical timescale (Table 5), which implies that coagulation will continue to be controlled by the ageing of fluid parcels or the mean tracer age. The dynamical timescales change with the wind direction (Supplementary Material, Table S-1), but the coagulation timescale, τ_{coag}, remains much longer. For stratified flow, the MTA will decrease for unstable stratification and increase for stable stratification but the effect should be relatively small (see Duan and Ngan (2019) for building array results). The situation is more complicated for deposition insofar as τ_{depo} is not much less than the relevant dynamical timescale, i.e., the canyon circulation timescale T_c. Qualitatively different behaviour is expected only for a much smaller T_c, such as may occur for unstable flow or a street canyon with lateral openings. In this case, deposition will be less spatially localised and will no longer proceed to completion. For cooking emissions, the relative contribution of deposition would therefore decrease compared to the cases examined in this paper, for which $\tau_{depo}/T_c < 1$.

A highly simplified representation of indoor aerosol processes was adopted. Since details of the kitchen ventilation systems and exhaust ducts vary, we focused on a configuration in which indoor aerosol processes and the effects of the ventilation system are ignored: it is assumed that all cooking-generated particles escape without loss, modification or re-entrainment. The results described in this study therefore correspond to an idealised but important limit. Given the fairly weak sensitivity to source flux and source location, one may expect that the results will not be greatly affected by the indoor aerosol processes unless there is a significant change in the emission strength or spectrum. The characteristic timescales for the outdoor aerosol processes (Fig. 13) suggest that the effects of indoor coagulation and deposition could be relatively weak; however, detailed analysis of ventilation systems would be required to quantify the effect. Calculations including an urban background derived from real urban measurements show that the spatial structure of the aerosol processes is essentially independent of the background spectrum. Moreover, the quantitative effect on the relative differences is small compared to the change in the total particle number.

The assumptions described above may partially explain why the mass concentrations (Appendix D) are very high. For example, concentrations would decrease if the assumption of perfect ventilation to the exterior were relaxed.

7   Conclusions

Cooking-generated aerosols differ significantly from traffic-generated ones. Using standard emission spectra and plausible assumptions about the traffic volume and restaurant dimensions, it was found that the number concentration within a unit-aspect-ratio street canyon is $\sim 50 - 100\%$ higher for boiling and deep frying than for traffic. This reflects differences in the

emission factors and the increased importance of deposition and coagulation. The latter is especially important for deep frying, which generates many small particles with diameter $D_p < 50$ nm. The results support the finding that organic aerosols may be determined primarily by cooking emissions in neighbourhoods with many restaurants (Lee et al., 2015; Liu et al., 2018). Even larger differences are seen in the mass concentration, though the effect of aerosol processes on PM2.5 is much smaller.

The sensitivity of the results to the source spectrum and source location can be understood by analysing the deposition and coagulation timescales. For the different cooking-emission scenarios, both timescales are comparable to or longer than the characteristic timescale for large-scale motions within the canyon. The upshot is that deposition is enhanced within corner vortices while coagulation occurs following fluid trajectories. The mean tracer age, which characterises the ageing of particles released at the source, reveals the spatial structure of coagulation.

The present study is restricted to idealised flow and emission scenarios. It would be instructive to perform a similar study for a real street canyon that contains restaurants. This would enable the impact of assumptions about the kitchen emission factors or the neglect of heated plumes to be assessed. However, in situ measurements, preferably of the size spectrum, would be required.

Appendix A: Aerosol parameterisations

A.1 Deposition

Dry deposition occurs when particles impact and stick to a solid surface. Many schemes have been developed for calculating the dry deposition velocity, v_d. In SALSA, the scheme of Zhang et al. (2001) is applied:

$$v_d = v_g + \frac{1}{R_a + R_s}, \tag{A1a}$$

$$u_g = \frac{\rho d_p^2 g C}{18\eta}, \tag{A1b}$$

$$R_a = \frac{\ln z_R/z_0 - \psi_H}{\kappa u_*}, \tag{A1c}$$

$$\frac{1}{R_s} = \varepsilon_0 u_* \left(Sc^{-\gamma} + \left(\frac{St}{0.8 + St} \right)^2 + \frac{1}{2} \left(\frac{d_p}{A} \right)^2 \right) R_1, \tag{A1d}$$

where v_g is the gravitational settling velocity; R_a and R_s represent the aerodynamic resistance and surface resistance, respectively; ρ is the particle density; g is the acceleration of gravity; η is the viscosity; and C is a correction factor. In Eq. A1c, z_R is the height, z_0 is the roughness length, u_* is the friction velocity, ψ_H is the stability function, and κ is the von Karman constant. For LES, u_* is estimated by $\sqrt{C_D U}$, where C_D is the drag coefficient and U is the local velocity magnitude. Sc is the particle Schmidt number and St is the Stokes number. ε_0, γ and A are constants based on the surface type.

A.2 Coagulation

Coagulation occurs when two particles collide and form a larger one. Following Jacobson and Jacobson (2005), the number concentration for size bin i is given by

$$n_{i,t} = \frac{n_{i,t-\Delta t} + \frac{1}{2}\Delta t \sum_{j=1}^{i-1} \beta_{i-j} n_{i-j} n_{j,t-\Delta t}}{1 + \Delta t \sum_{j=1}^{\infty} \beta_{i,j} n_{j,t-\Delta t}} \tag{A2}$$

where δ_t is the time step and β represents the coagulation kernel ($\mathrm{cm^3\,particle^{-1}\,s^{-1}}$) for particles in size bins i and j. The coagulation kernel or rate coefficient is calculated as

$$\beta_{i,j} = \frac{4\pi(r_i+r_j)(D_i+D_j)}{\frac{r_i+r_j}{r_i+r_j+(\delta_i^2+\delta_j^2)^{1/2}} + \frac{4(D_i+D_j)}{(\overline{\nu_{pi}}^2 + \overline{\nu_{pj}}^2)^{1/2}(r_i+r_j)}} . \tag{A3}$$

Here, D is the particle diffusion coefficient; δ denotes the mean distance from the centre of a sphere defined by the particle mean free path, λ_{pi}; $\overline{\nu_p}$ is the thermal velocity.

A.3 Condensation

Condensation increases the particle volume through mass transfer. Following Jacobson and Jacobson (2005), the vapour mole concentration of a condensing gas g is calculated as

$$C_{g,t} = \frac{C_{g,t-\Delta t} + \Delta t \sum_{i=1}^{N}(k_{g,i,t-\Delta t} S'_{g,i,t-\Delta t} C_{g,s,i,t-\Delta t})}{1 + \Delta t \sum_{i=1}^{N} k_{g,i,t-\Delta t}}, \tag{A4}$$

whence the particle mole concentration may be updated,

$$c_{g,i,t} = c_{g,i,t-\Delta t} + \Delta t k_{g,i,t-\Delta t}(C_{g,t} - S'_{g,i,t-\Delta t} C_{g,s,i,t-\Delta t}). \tag{A5}$$

Here, $k_{g,i,t-\Delta t}$ is the mass-transfer coefficient ($\mathrm{s^{-1}}$); $S'_{g,i,t-\Delta t}$ is the equilibrium saturation ratio; and $C_{g,s,i,t-\Delta t}$ is the uncorrected saturation vapour mole concentration ($\mathrm{mol\,m^{-3}}$).

Appendix B: Chemical compositions and emission factors for gaseous compounds

Table B-1. Chemical compositions for cooking (See and Balasubramanian, 2008) and traffic (Yubero et al., 2015) emissions. In the former case, a gas stove is assumed.

	Composition(%)	Mass ($\mu g\,m^{-3}$)	OC	BC	Cl–	NO_3^-	SO_4^-	NH_4^+
Cooking	Deep-frying	82.3 ± 40.8	60.8	7.3	0.21	3.5	0.5	0.3
	Boiling	40.9 ± 11.8	43.0	8.5	2.9	7.3	1.8	0.3
	Traffic		43.0	17.5	0.0	5.0	24.8	9.7

Table B-2. Gaseous emission factors for cooking (Shen et al., 2018) and traffic (Kumar et al., 2008) emissions. In the latter case, the emission factors are derived by assuming that that there is one stove for a kitchen of volume 16 m^3.

	H_2SO_4	HNO_3	NH_3	NVOC	SVOC
	$\mathrm{g\,km^{-1}\,veh^{-1}}$				
Traffic	2.5×10^{-4}	0.0	4.2×10^{-2}	0.0	2.5×10^{-3}
	$\mathrm{g\,min^{-1}}$				
Cooking	0.0	3.8×10^{-3}	0.0	0.0	5.5×10^{-4}

Appendix C: Validation of scalar statistics

495 Time-averaged concentration statistics are compared with the wind-tunnel data of Pavageau and Schatzmann (1999) by intro-ducing a ground-level line source along the central axis of the unit-aspect-ratio street canyon. The numerical configuration is otherwise unchanged from Sect. 2.3. Fig. C-1 shows normalised concentration profiles at different streamwise positions. Concentrations are consistently overpredicted at the leeward wall, centre and windward wall; however, the agreement is at least as good as the previous LES validation of Michioka et al. (2011). In order to quantify the agreement, standard air quality metrics

500 (Chang and Hanna, 2004) are calculated:

$$\mathrm{FB} = \frac{\overline{C_o} - \overline{C_p}}{0.5(\overline{C_o} + \overline{C_p})}, \tag{C1}$$

$$\mathrm{NMSE} = \frac{\overline{(C_o - C_p)^2}}{\overline{C_o}\overline{C_p}}, \tag{C2}$$

where C_p and C_o denote the model predictions and observations, respectively. A perfect model would have $\mathrm{FB} = \mathrm{NMSE} = 0$. For the validation, $NSME = 0.07$ and $FB = 0.2$, indicating relatively good agreement. We conclude that the model is capable

505 of predicting mean concentrations for a passive scalar within a street canyon.
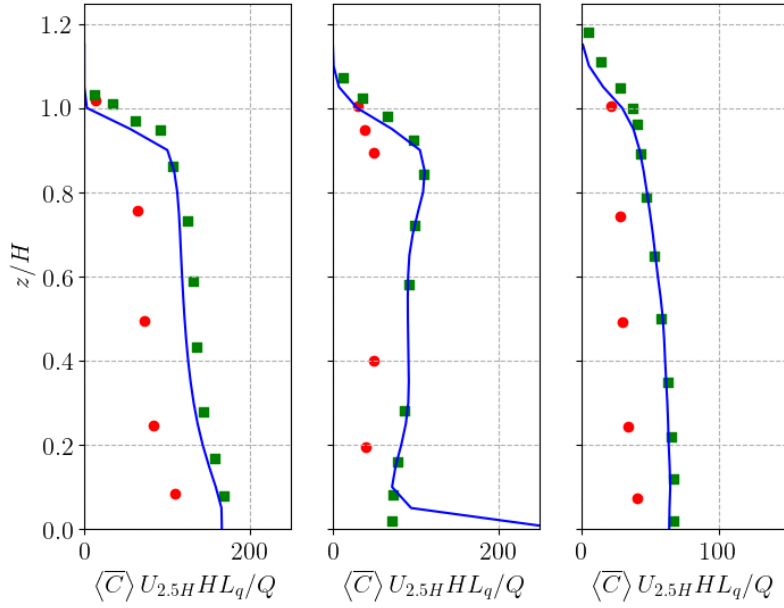
Figure C-1. Vertical profiles of the normalised mean concentration plotted at x/W = -0.5, 0 and 0.5. The results from present LES simulations are plotted in blue lines and are compared with wind-tunnel data from Pavageau and Schatzmann (1999) (red circles) and LES data from Michioka et al. (2011) (green squares). $U_{2.5H}$ denotes the the temporal and spatial average of the streamwise velocity at z/H = 2.5 and Q is the source flux.

Appendix D: Mass concentrations

Mean mass concentration fields for traffic and near-ground emissions are plotted in Fig. D-1.
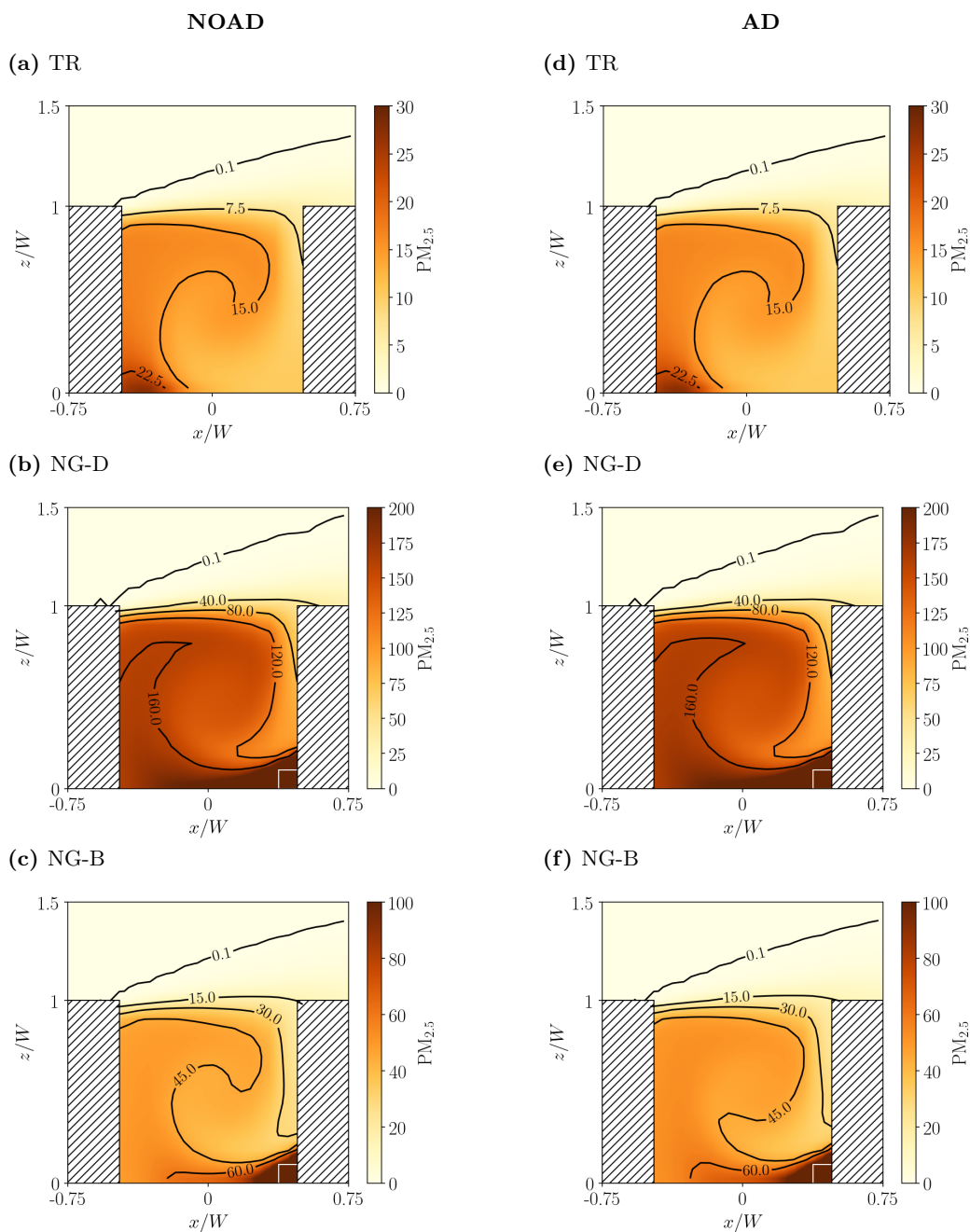
Figure D-1. As in Fig. 6, but for PM2.5 concentrations. The mass concentrations are largely insensitive to aerosol dynamic processes.

Appendix E: Calculation of the mean tracer age

The mean tracer age measures the time elapsed from the release of a passive scalar at a source location to its arrival at the receptor. The theory is described in Holzer and Hall (2000) and Lo and Ngan (2015). Briefly, a Green's function, $G(\mathbf{x}|\mathbf{x}_0)$, which maps the scalar concentration from the source $\mathbf{x}_0$ to the receptor $\mathbf{x}$, is obtained from the solution of the advection-diffusion equation for an impulse source (i.e. delta function in time). The age spectrum or probability distribution, Z, of transit times, ξ, is given by

$$Z(\mathbf{x},\xi) = \frac{\int_D G(\mathbf{x},\xi|\mathbf{x_0})S(\mathbf{x}_0)d\mathbf{x_0}}{c(\mathbf{x},t)}, \tag{E1}$$

where S refers to the source and c is the concentration. The mean tracer age is the first moment of the age spectrum, i.e.

$$\tau_{MTA} = \int_0^\infty \xi Z d\xi. \tag{E2}$$

Appendix F: Measurements of the background size spectrum

The measurements were conducted from 1 to 8 March 13:00-18:00 local time on the roof of Hoi Pa Street Government Primary School, Tsuen Wan, Hong Kong (height: 31 m, coordinates: 22.372° N, 114.115°E, Fig. F-1). Using a Kanomax PAMS 3300 spectrometer and 14 fixed channels, the number distribution was measured from 14.51 nm to 862.32 nm. The number spectra (75 in total) were averaged to yield the spectrum of Fig. 15d. The site is located in a suburban neighbourhood. During the measurement period, the average traffic volume along the main road (Tai Ho Road) was 2050 veh/h. The mean number concentration, $\bar{N} = 2.3 \times 10^{10}\,\mathrm{m}^{-3}$, implying $N_b = 0.5N_0$, where N_0 is the mean canyon-averaged number concentration for NG-B.
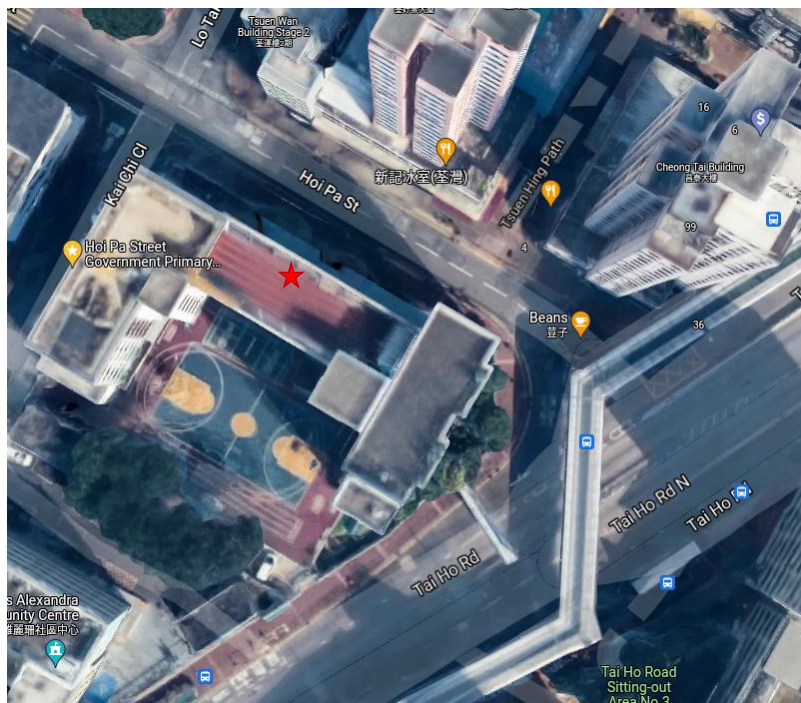
Figure F-1. Measurement site in Tseun Wan, Hong Kong (image taken from © Google Maps). The measurement location is indicated by the red star.

525 *Acknowledgements.* Financial support was provided by the Environmental and Conservation Fund (Project 7/2020), Guangzhou Development District International Science and Technology Cooperation Project (No. 2018GH08), and City University of Hong Kong (Project 7005283). The authors thank Alvin CK Lai for lending the portable spectrometer.

Code availability. The codes used in this publication are available to the community, and they can be accessed by request to the corresponding author.

530 *Author contributions.* SG conducted the simulations with MK developing the model code. SG analysed the data. SG, KN and CKC wrote the paper. All co-authors contributed to the discussion of the paper.

Competing interests. The authors declare that they have no conflict of interest.

References

Ackerman, A. S., Toon, O. B., and Hobbs, P. V.: Numerical modeling of ship tracks produced by injections of cloud condensation nuclei into marine stratiform clouds, J. Geophys. Res.: Atmos., 100, 7121–7133, 1995.

Baik, J.-J., Kang, Y.-S., and Kim, J.-J.: Modeling reactive pollutant dispersion in an urban street canyon, Atmos. Environ., 41, 934–949, 2007.

Brown, M. J., Lawson, R. E., DeCroix, D. S., Lee, R., et al.: Comparison of centerline velocity measurements obtained around 2D and 3D building arrays in a wind tunnel, Int. Soc. Environ. Hydraulics, Tempe, AZ, 5, 2001.

Chang, J. C. and Hanna, S. R.: Air quality model performance evaluation, Meteorol. Atmos. Phys., 87, 167–196, 2004.

Cui, Z., Cai, X., and J. Baker, C.: Large-eddy simulation of turbulent flow in a street canyon, Q. J. R. Meteorolog. Soc., 130, 1373–1394, 2004.

Deardorff, J. W.: Stratocumulus-capped mixed layers derived from a three-dimensional model, Boundary Layer Meteorol., 18, 495–527, 1980.

Duan, G. and Ngan, K.: Sensitivity of turbulent flow around a 3-D building array to urban boundary-layer stability, J. Wind Eng. Ind. Aerodyn., 193, 103 958, 2019.

Duan, G., Jackson, J., and Ngan, K.: Scalar mixing in an urban canyon, Environ. Fluid Mech., 19, 911–939, 2019.

Fujitani, Y., Takahashi, K., Fushimi, A., Hasegawa, S., Kondo, Y., Tanabe, K., and Kobayashi, S.: Particle number emission factors from diesel trucks at a traffic intersection: Long-term trend and relation to particle mass-based emission regulation, Atmos. Environ.: X, 5, 100 055, 2020.

Gao, J., Jian, Y., Cao, C., Chen, L., and Zhang, X.: Indoor emission, dispersion and exposure of total particle-bound polycyclic aromatic hydrocarbons during cooking, Atmos. Environ., 120, 191–199, 2015.

Gong, S., Barrie, L., and Lazare, M.: Canadian Aerosol Module (CAM): A size-segregated simulation of atmospheric aerosol processes for climate and air quality models 2. Global sea-salt aerosol and its budgets, J. Geophys. Res.: Atmos., 107, AAC–13, 2002.

Greene, N. A. and Morris, V. R.: Assessment of public health risks associated with atmospheric exposure to PM2. 5 in Washington, DC, USA, Int. J. Environ. Res. Public Health, 3, 86–97, 2006.

Harrison, R. M.: Urban atmospheric chemistry: a very special case for study, npj Climate and Atmospheric Science, 1, 20 175, https://doi.org/10.1038/s41612-017-0010-8, 2018.

Holzer, M. and Hall, T. M.: Transit-time and tracer-age distributions in geophysical flows, J. Atmos. Sci., 57, 3539–3558, 2000.

Huang, Y.-d., Xu, X., Liu, Z.-Y., and Kim, C.-N.: Effects of Strength and Position of Pollutant Source on Pollutant Dispersion Within an Urban Street Canyon, Environ. Forensics, 16, 163–172, 2015.

Jacobson, M. Z. and Jacobson, M. Z.: Fundamentals of atmospheric modeling, Cambridge university press, 2005.

Janhäll, S., Jonsson, Å. M., Molnár, P., Svensson, E. A., and Hallquist, M.: Size resolved traffic emission factors of submicrometer particles, Atmos. Environ., 38, 4331–4340, 2004.

Karl, M., Kukkonen, J., Keuken, M. P., Lützenkirchen, S., Pirjola, L., and Hussein, T.: Modeling and measurements of urban aerosol processes on the neighborhood scale in Rotterdam, Oslo and Helsinki, Atmos. Chem. Phys., 16, 4817–4835, 2016.

Ketzel, M. and Berkowicz, R.: Modelling the fate of ultrafine particles from exhaust pipe to rural background: an analysis of time scales for dilution, coagulation and deposition, Atmos. Environ., 38, 2639–2652, 2004.

Kim, M. J., Park, R. J., and Kim, J.-J.: Urban air quality modeling with full O3–NOx–VOC chemistry: Implications for O3 and PM air quality in a street canyon, Atmos. Environ., 47, 330–340, 2012.

Kim, M. J., Park, R. J., Kim, J.-J., Park, S. H., Chang, L.-S., Lee, D.-G., and Choi, J.-Y.: Computational fluid dynamics simulation of reactive fine particulate matter in a street canyon, Atmos. Environ., 209, 54–66, 2019.

Kokkola, H., Korhonen, H., Lehtinen, K., Makkonen, R., Asmi, A., Järvenoja, S., Anttila, T., Partanen, A.-I., Kulmala, M., Järvinen, H., et al.: SALSA–a sectional aerosol module for large scale applications, Atmos. Chem. Phys., 8, 2469–2483, 2008.

Kumar, P., Fennell, P., and Britter, R.: Measurements of particles in the 5–1000 nm range close to road level in an urban street canyon, Sci. Total Environ., 390, 437–447, 2008.

Kumar, P., Ketzel, M., Vardoulakis, S., Pirjola, L., and Britter, R.: Dynamics and dispersion modelling of nanoparticles from road traffic in the urban atmospheric environment—a review, J. Aerosol Sci., 42, 580–603, 2011.

Kurppa, M., Hellsten, A., Roldin, P., Kokkola, H., Tonttila, J., Auvinen, M., Kent, C., Kumar, P., Maronga, B., and Järvi, L.: Implementation of the sectional aerosol module SALSA2.0 into the PALM model system 6.0: model development and first evaluation, Geosci. Model Dev., 12, 1403–1422, 2019.

Lee, B. P., Li, Y. J., Yu, J. Z., Louie, P. K., and Chan, C. K.: Characteristics of submicron particulate matter at the urban roadside in downtown Hong Kong—Overview of 4 months of continuous high-resolution aerosol mass spectrometer measurements, J. Geophys. Res.: Atmos., 120, 7040–7058, 2015.

Liu, T., Wang, Z., Huang, D. D., Wang, X., and Chan, C. K.: Significant production of secondary organic aerosol from emissions of heated cooking oils, Environ. Sci. Technol. Lett., 5, 32–37, 2018.

Lo, K. and Ngan, K.: Characterising the pollutant ventilation characteristics of street canyons using the tracer age and age spectrum, Atmos. Environ., 122, 611–621, 2015.

Lo, K. W. and Ngan, K.: Characterising urban ventilation and exposure using Lagrangian particles, Journal of Applied Meteorology and Climatology, 56, 1177–1194, https://doi.org/10.1175/JAMC-D-16-0168.1, 2017.

Maronga, B., Gryschka, M., Heinze, R., Hoffmann, F., Kanani-Sühring, F., Keck, M., Ketelsen, K., Letzel, M. O., Sühring, M., and Raasch, S.: The Parallelized Large-Eddy Simulation Model (PALM) version 4.0 for atmospheric and oceanic flows: model formulation, recent developments, and future perspectives, Geosci. Model Dev., 8, 2515–2551, 2015.

Melli, P. and Runca, E.: Gaussian plume model parameters for ground-level and elevated sources derived from the atmospheric diffusion equation in a neutral case, J. Appl Meteorol. Clim, 18, 1216–1221, 1979.

Michioka, T., Sato, A., Takimoto, H., and Kanda, M.: Large-eddy simulation for the mechanism of pollutant removal from a two-dimensional street canyon, Bound.-Layer Meteorol., 138, 195–213, 2011.

Nazarian, N. and Kleissl, J.: Realistic solar heating in urban areas: air exchange and street-canyon ventilation, Build. Environ., 95, 75–93, 2016.

Nikolova, I., Janssen, S., Vos, P., Vrancken, K., Mishra, V., and Berghmans, P.: Dispersion modelling of traffic induced ultrafine particles in a street canyon in Antwerp, Belgium and comparison with observations, Sci. Total Environ., 412, 336–343, 2011.

Park, S.-B., Baik, J.-J., and Lee, S.-H.: Impacts of mesoscale wind on turbulent flow and ventilation in a densely built-up urban area, J. Appl Meteorol. Clim, 54, 811–824, 2015.

Pavageau, M. and Schatzmann, M.: Wind tunnel measurements of concentration fluctuations in an urban street canyon, Atmos. Environ., 33, 3961–3971, 1999.

Purba, L. P. and Tekasakul, P.: Computational fluid dynamics study of flow and aerosol concentration patterns in a ribbed smoked sheet rubber factory, Part. Sci. Technol., 30, 220–237, 2012.

Rivas, E., Santiago, J. L., Lechón, Y., Martín, F., Ariño, A., Pons, J. J., and Santamaría, J. M.: CFD modelling of air quality in Pamplona City (Spain): Assessment, stations spatial representativeness and health impacts valuation, Sci. Total Environ., 649, 1362–1380, 2019.

610 Rönkkö, T., Virtanen, A., Kannosto, J., Keskinen, J., Lappi, M., and Pirjola, L.: Nucleation Mode Particles with a Nonvolatile Core in the Exhaust of a Heavy Duty Diesel Vehicle, Environ. Sci. Technol., 41, 6384–6389, https://doi.org/10.1021/es0705339, 2007.

Scungio, M., Arpino, F., Stabile, L., Buonanno, G., et al.: Numerical simulation of ultrafine particle dispersion in urban street canyons with the Spalart-Allmaras turbulence model, Aerosol Air Qual. Res., 13, 1423–1437, 2013.

See, S. W. and Balasubramanian, R.: Physical characteristics of ultrafine particles emitted from different gas cooking methods, Aerosol Air 615 Qual. Res., 6, 82–92, 2006.

See, S. W. and Balasubramanian, R.: Chemical characteristics of fine particles emitted from different gas cooking methods, Atmos. Environ., 42, 8852–8862, 2008.

Seinfeld, J. H. and Pandis, S. N.: Atmospheric chemistry and physics: from air pollution to climate change, John Wiley & Sons, 2016.

Shen, G., Hays, M. D., Smith, K. R., Williams, C., Faircloth, J. W., and Jetter, J. J.: Evaluating the performance of household liquefied 620 petroleum gas cookstoves, Environ. Sci. Technol., 52, 904–915, 2018.

Wicker, L. J. and Skamarock, W. C.: Time-splitting methods for elastic models using forward time schemes, Mon. Weather Rev., 130, 2088–2097, 2002.

Williamson, J.: Low-storage Runge-Kutta schemes, J. Comput. Phys., 35, 48–56, 1980.

Yeung, L. and To, W.: Size distributions of the aerosols emitted from commercial cooking processes, Indoor Built Environ., 17, 220–229, 625 2008.

Yubero, E., Galindo, N., Nicolás, J., Crespo, J., Calzolai, G., and Lucarelli, F.: Temporal variations of PM 1 major components in an urban street canyon, Environ. Sci. Pollut. Res., 22, 13 328–13 335, 2015.

Zhang, L., Gong, S., Padro, J., and Barrie, L.: A size-segregated particle dry deposition scheme for an atmospheric aerosol module, Atmos. Environ., 35, 549–560, 2001.

630 Zhang, Y.-W., Gu, Z.-L., Lee, S.-C., Fu, T.-M., and Ho, K.-F.: Numerical simulation and in situ investigation of fine particle dispersion in an actual deep street canyon in Hong Kong, Indoor Built Environ., 20, 206–216, 2011.

Zhong, J., Cai, X.-M., and Bloss, W. J.: Modelling the dispersion and transport of reactive pollutants in a deep urban street canyon: Using large-eddy simulation, Environ. Pollut., 200, 42–52, 2015.